

The Impact of Stochastic Wavefunction Evolution in Dispersively Measured Bose-Einstein Condensates

Emine Altuntas* and I. B. Spielman†

*Joint Quantum Institute, National Institute of Standards and Technology,
and University of Maryland, Gaithersburg, Maryland, 20899, USA*

(Dated: September 12, 2022)

A fundamental tenet of quantum mechanics is that measurements change a system’s wavefunction to that most consistent with the measurement outcome, even if no observer is present. Weak measurements—termed partial or non-destructive in different settings—produce only limited information about the system, and as a result only minimally change the system’s state. Here, we theoretically and experimentally characterize quantum back-action in atomic Bose-Einstein condensates (BECs), weakly measured by the light scattered from a far-from resonant, i.e., dispersively interacting, probe laser beam. We theoretically describe this process using a quantum trajectories approach and present a measurement model based on an ideal photodetection mechanism. We experimentally quantify the resulting wavefunction change with three observations: the change in total atom number, the contrast of a Ramsey interferometer, and the deposited energy. Further, we demonstrate control over parasitic effects associated with the measurement process: probe-induced photoassociation (an intrinsic atomic process), as well as stray optical lattices (a technical consequence of weak retro-reflections). The observed back-action is in good agreement with our measurement model, enabling true quantum back-action limited measurements of BECs.

Quantum trajectories provide a robust framework for understanding weakly measured quantum systems [1, 2]. In these descriptions, the system and a larger reservoir interact and become weakly entangled, at which point the reservoir is projectively measured. This destroys the system-reservoir (SR) entanglement and leads to a change in the system’s wavefunction conditioned on the measurement outcome, i.e., back-action. Real-time quantum control via subsequent classical feedback can be a powerful tool for establishing and maintaining quantum coherence and entanglement, with applications ranging from quantum state preparation [3, 4] to quantum error correction [5]. Even without feedback, system dynamics combined with weak measurements can lead to entangled states in the thermodynamic limit [6–9]. Large-scale applications of these capabilities hinge on understanding system-reservoir dynamics of many-body quantum systems, whose Hilbert space grows exponentially with system size. Ultracold atoms, a workhorse for quantum simulation [10, 11], are an ideal platform for studying the system-reservoir dynamics of large-scale many-body systems.

Here, we characterize measurement back-action in atomic Bose-Einstein condensates (BECs), weakly interacting with a far-from resonant laser beam. We develop a theoretical measurement model rooted in quantum trajectory techniques to study the interplay between the system-reservoir interaction, the scattered light, and the post-measurement system state. We demonstrate that both intrinsic effects and technical artifacts associated with the measurement process can be eliminated, bringing the observed back-action into agreement with our

measurement model.

Very far from atomic resonance light Rayleigh-scatters from atomic ensembles, changing the incident light’s wavevector in proportion to the Fourier transform of the atomic density distribution. The straightforward interpretation of back-action resulting from scattered photons makes quantum trajectories an ideal tool for both intuitively and quantitatively understanding the system-reservoir interaction. In the quantum problem, light scattering gives information both about the expectation value of the density—essentially classical scattering—as well as quantum fluctuations, which contribute to spontaneous emission. Quite recently a trio of papers observed the predicted suppression of light-scattering from deeply degenerate Fermi gases [12–14] as well as amplification from ultracold Bose gases [15]; these effects result from scattering atoms into occupied quantum states (unsuccessfully in the case of Fermi gases). Here we focus on the information extracted by light-scattering as a quantum measurement process where the scattered light is detected by the environment, and we detect only the associated back-action on the system. We quantify the resulting wavefunction change with three observations: first, the change in atom number; second, the phase shift and contrast of a Ramsey interferometer in which only one of the spin states is measured; and third, the deposited energy.

The latter two of these measurements can be described simply from a measurement paradigm. In the case of Ramsey interferometry, spontaneously scattered light measures atoms to be in the detected spin state, thereby breaking its coherence and reducing the interferometer contrast. In the case of heating, the measurement defines the momentum of atoms scattered by light, and thereby the added energy. Neither of these observations rely on knowledge of the particular quantum trajectory the system followed. When the reservoir-measurement out-

* altuntas@umd.edu

† ian.spielman@nist.gov

comes are rejected, quantum trajectories methods form a specific physically motivated “unraveling” of the master equation [2].

Ultracold atoms have multiple well-established “non-destructive” measurement techniques [16–20] that allow for real-time [21, 22] readout. Previous demonstrations of such non-destructive measurement methods thus far lacked a comprehensive study of the quantum back-action. A central part of our work distinguishes between non-destructive measurements (where the system is apparently undisturbed by the measurement) and back-action limited measurements (where quantum projection noise dominates the change in the post-measurement state). We systematically control for stray effects that otherwise lead to excess excitation or loss. In particular, we identify and suppress three primary effects: photoassociation (PA), an intrinsic effect induced by the probe beam; inhomogeneities in the probe beam; and a weak optical lattice from weak back-reflections. The latter two are technical artifacts.

This paper begins by formulating our measurement-based theoretical framework in Sec. I. Next, in Sec. II, we continue with a brief description of our experimental setup and elaborate on measurement-induced atom loss as a prefatory indicator of measurement back-action. In Sec. III, we move on to Ramsey interferometry measurements and establish that, in conjunction with experimental control of systematic effects, our measurement model accurately describes the observed Ramsey contrast. In Sec. IV, we study measurement induced heating. Section V concludes with a discussion of experimental and theoretical implications, and describes potential future directions for research.

I. QUANTUM TRAJECTORIES

We consider a weakly interacting atomic BEC (the system) dispersively coupled to the optical electric field $\hat{\mathbf{E}}(\mathbf{x}, t)$ (the reservoir) by the ac Stark shift with interaction picture Hamiltonian

$$\hat{H}_{\text{SR}}(t) = \int \frac{d^3 \mathbf{x}}{\hbar \Delta} \hat{n}_g(\mathbf{x}) \otimes [\hat{\mathbf{E}}(\mathbf{x}, t) \cdot \mathbf{d}_{\text{ge}}] [\mathbf{d}_{\text{ge}}^* \cdot \hat{\mathbf{E}}^\dagger(\mathbf{x}, t)]. \quad (1)$$

Here $\hat{n}_g(\mathbf{x}) = \hat{b}_g^\dagger(\mathbf{x}) \hat{b}_g(\mathbf{x})$ is the atomic density operator in terms of the bosonic field operators $\hat{b}_g(\mathbf{x})$ for ground state atoms at position \mathbf{x} ; \mathbf{d}_{ge} is the dipole matrix element for transitions between ground and excited state atoms with energy difference $\hbar\omega_{\text{ge}}$; lastly, $\Delta = \omega_0 - \omega_{\text{ge}}$ is the detuning from atomic resonance of a probe laser with frequency ω_0 .

For $|\Delta| \ll \omega_{\text{ge}}$, the optical electric field operator is

$$\hat{\mathbf{E}}(\mathbf{x}, t) = i \sqrt{\frac{\hbar\omega_{\text{ge}}}{2\epsilon_0}} \sum_{\sigma} \int \frac{d^3 \mathbf{k}}{(2\pi)^3} \hat{a}_{\sigma}(\mathbf{k}) \epsilon_{\sigma}(\mathbf{k}) e^{i(\mathbf{k} \cdot \mathbf{x} - c|\mathbf{k}|t)}, \quad (2)$$

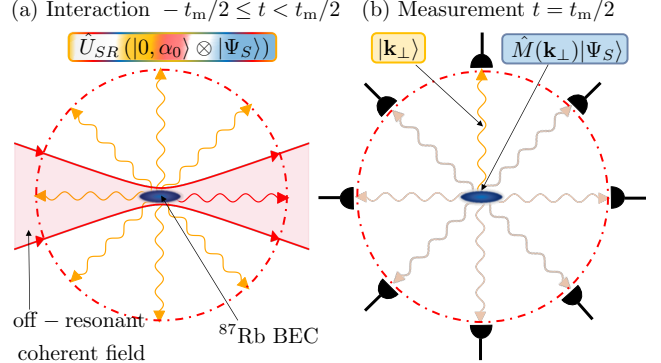


FIG. 1. Measurement model. (a) Interaction. BEC (blue) is illuminated with far-detuned laser light (red) for a time t_m and scatters light (wiggly lines) into both occupied (red) and reservoir (orange) modes. (b) Measurement. The reservoir modes are projectively measured by an array of photodetectors encompassing 4π steradians yielding the outgoing wavevector and polarization. In this example a photon in state $|\mathbf{k}_f, \sigma_f\rangle$ was detected leading to the conditional update of the system $|\Psi'\rangle = \hat{M}(\mathbf{k}_\perp) |\Psi_S\rangle$.

expressed in terms of field operators $\hat{a}_{\sigma}(\mathbf{k})$ describing states with wavevector \mathbf{k} and polarization σ . Here, c is the speed of light; ϵ_0 is the electric constant; and $\epsilon_{\sigma}(\mathbf{k})$ are a pair orthogonal polarization vectors transverse to \mathbf{k} , labeled by $\sigma = \pm$. Figure 1(a) depicts the full system-reservoir coupling scheme with the BEC interacting with outgoing transverse modes and a probe laser in mode (\mathbf{k}_0, σ_0) for a duration t_m .

During this time the atomic ensemble scatters monochromatic light into outgoing modes of wavevector \mathbf{k}_\perp with coupling strength

$$g_{\sigma}(\mathbf{k}_\perp) \equiv -i \left(\frac{\omega_{\text{ge}}}{2\hbar\epsilon_0} \right)^{1/2} [\mathbf{d}_{\text{ge}} \cdot \epsilon_{\sigma}(\mathbf{k}_\perp)]. \quad (3)$$

Since each outgoing mode is in a specific polarization state $\epsilon(\mathbf{k}_\perp)$ the polarization subscript is redundant.

Assuming that the probe laser of wavelength λ occupies a single optical mode (\mathbf{k}_0, σ_0) with $k_0 \equiv |\mathbf{k}_0| = 2\pi/\lambda$, we make the replacement $\hat{a}_{\sigma}(\mathbf{k}) \rightarrow \delta(\mathbf{k} - \mathbf{k}_0) \delta_{\sigma, \sigma_0} \alpha_0 + \hat{a}_{\sigma}(\mathbf{k})$, which describes a coherent driving field with amplitude α_0 . In this expression the modes $\hat{a}_{\sigma}(\mathbf{k})$ are initially empty. This replacement allows us to expand Eq. (1) in decreasing powers of the large parameter α_0 . The leading term describes the ac Stark shift, and the next term

$$\hat{H}_{\text{eff}} = \frac{\hbar P_e^{1/2}}{(ct_m)^{1/2}} \int_{k_0} \frac{d^2 \mathbf{k}_\perp}{(2\pi)^2} g^*(\mathbf{k}_\perp) \hat{n}_{\mathcal{F}}(\mathbf{k}_\perp - \mathbf{k}_0) \hat{a}^\dagger(\mathbf{k}_\perp) + \text{H.c.}$$

describes scattering from the probe field into modes by any structure in the atomic density, with Fourier components

$$\hat{n}_{\mathcal{F}}(\mathbf{k}_\perp - \mathbf{k}_0) = \int \frac{d^3 \mathbf{k}}{(2\pi)^3} \hat{b}^\dagger[\mathbf{k} - (\mathbf{k}_\perp - \mathbf{k}_0)] \hat{b}(\mathbf{k}).$$

Here $P_e = |\alpha_0 g_{\sigma_0}(\mathbf{k}_0)|^2 / \Delta^2$ is the excited state occupation probability. In the far-detuned limit, the outgoing

wavenumber is fixed at k_0 leading to the surface integral over the sphere of radius k_0 .

We model the larger environment as performing measurements on the outgoing light in the far-field with an ideal photo detection process, a strong measurement of the photon density $\hat{a}^\dagger(\mathbf{k})\hat{a}(\mathbf{k})$. In the abstract, this process begins with the combined system reservoir state $|0\rangle \otimes |\Psi_S\rangle$, describing a reservoir with no photons but with the system in an arbitrary state. This state evolves briefly for a time t_m via the time evolution operator $\hat{U}_{SR}(t_m) = \mathcal{T} \exp \left[-i \int_{-t_m/2}^{t_m/2} \hat{H}_{\text{eff}}(t) dt / \hbar \right]$. This entangles the system and reservoir; as depicted in Fig. 1(a) amplitude can be present in every reservoir mode prior to measurement by the environment.

A. Photodetection Model

We turn to the photodetection model shown in Fig. 1(b). In this case, the measurement of the reservoir collapses the superposition by measuring either no photons or a single photon in final state $|\mathbf{k}_\perp\rangle$. The back-action of this measurement is described by a conditional change in the system wavefunction $|\Psi'_S\rangle = \hat{M}(\mathbf{k}_\perp)|\Psi_S\rangle$, an operation described by Kraus operator $\hat{M}(\mathbf{k}_\perp) = \langle \mathbf{k}_\perp | \hat{U}_{SR}(t_m) | 0 \rangle$. Taken together this schema is a generalized measurement of the system effected by projective measurements on the reservoir.

In the limit of small t_m , such that at most one photon is scattered, we obtain the Kraus operator

$$\hat{M}(\mathbf{k}_\perp) = -i P_e^{1/2} \left(\frac{t_m}{c} \right)^{1/2} g^*(\mathbf{k}_\perp) \hat{n}_{\mathcal{F}}(\mathbf{k}_\perp - \mathbf{k}_0) \quad (4)$$

describing the recoil of the system from momentum-conserving scattering out of every occupied state.

The Kraus operator contains information both about the change in the system as well as the probability density

$$\begin{aligned} P(\mathbf{k}_\perp) &\equiv \langle \Psi_S | \hat{M}^\dagger(\mathbf{k}_\perp) \hat{M}(\mathbf{k}_\perp) | \Psi_S \rangle \quad (5) \\ &= \frac{t_m P_e}{c} |g(\mathbf{k}_\perp)|^2 \langle \Psi_S | \hat{n}_{\mathcal{F}}(\mathbf{k}_0 - \mathbf{k}_\perp) |^2 | \Psi_S \rangle \end{aligned}$$

that this change occurred. Bringing $|\hat{n}_{\mathcal{F}}|^2$ into a normal-ordered form shows that the scattering probability has two contributions. For a BEC with condensate mode $\tilde{\psi}(\mathbf{k})$ the scattering probability is

$$P(\mathbf{k}_\perp) = \frac{t_m P_e}{c} |g(\mathbf{k}_\perp)|^2 N \left[(N-1) |n_{\mathcal{F}}(\mathbf{k}_0 - \mathbf{k}_\perp)|^2 + 1 \right],$$

where in analogy with the operator expression, $n_{\mathcal{F}}(\mathbf{k}_0 - \mathbf{k}_\perp)$ describes the Fourier components of the probability-density. The first term describes collective scattering from the overall density profile (including thermal fluctuations), a.k.a. classical scattering [23], while the second results from scattering from quantum fluctuations, here giving rise to spontaneous emission. For extended systems such as our BEC, the collective term is dominated

by small angle forward scattering while the spontaneous term is nominally isotropic. Notably, this result illustrates that the ratio between collective and spontaneous scattering depends on N but not the measurement parameters.

Integrating over the final \mathbf{k}_\perp states gives $P_{\text{tot}} = P_{\text{col}} + P_{\text{sp}}$ with the spontaneous scattering probability $P_{\text{sp}} = \Gamma t_m P_e = g^2/8$. We introduced an overall measurement strength $g = \sqrt{t_m \bar{I}/\bar{\delta}}$ in terms of dimensionless: time $\bar{t}_m = \Gamma t_m$ scaled by the natural linewidth Γ ; detuning $\bar{\delta} = \Delta/\Gamma$ in units of Γ ; and laser intensity $\bar{I} = I/I_{\text{sat}}$ in units of the saturation intensity I_{sat} . Thus when $g = \sqrt{8}$ each atom will have on average spontaneously scattered a single photon [App. B briefly discusses the relation between g and the signal to noise ratio (SNR) of a measurement outcome].

In experiment, a single measurement pulse can lead to thousands of photodetection events, each described by a Kraus operator. The concatenation of many such Kraus operators—one for each scattering event—describes the evolution of our system.

This analysis produces a quantum trajectories description of our physical system. We compare the predictions of this theoretical description with observables such as total atom number, contrast in a Ramsey interferometer, and change in total energy, that do not rely on knowledge of the specific quantum trajectory that the system followed.

II. PRELIMINARY MEASUREMENTS

A. Experimental System

Our experiments started with highly elongated ^{87}Rb BECs prepared in a crossed optical dipole trap (ODT) with frequencies $(\omega_x, \omega_y, \omega_z) = 2\pi \times [9.61(3), 113.9(3), 163.2(3)]$ Hz in the $|g_1\rangle \equiv |F=1, m_F=1\rangle$ electronic ground state [24]. This trap configuration yielded condensates with $N_c = 0.70(15) \times 10^5$ atoms [25, 26], condensate fraction $R_c = 78(3)\%$, and chemical potential $\mu = h \times 0.76(6)$ kHz. We drove transitions between $|g_1\rangle$ and $|g_2\rangle \equiv |F=2, m_F=2\rangle$ using an ≈ 6.8 GHz microwave magnetic field with Rabi frequency ≈ 7.5 kHz.

In our experiments we illuminated the BEC *in situ* or after a short time-of-flight (TOF) up to 5 ms with an off-resonant probe laser beam that drove the $|g_2\rangle$ to $|e\rangle \equiv |F'=3, m'_F=3\rangle$ ground to excited state transition. This probe laser was blue detuned by $0 < \bar{\delta} < 317$, and had intensity $\bar{I} \lesssim 10$. We theoretically describe the light scattered at large angle as being subsequently projectively measured by the environment, as described above. We then detected the post-measurement density distribution using absorption imaging after a long TOF during which a Stern-Gerlach gradient spatially separated the $|g_1\rangle$ and $|g_2\rangle$ components [27].

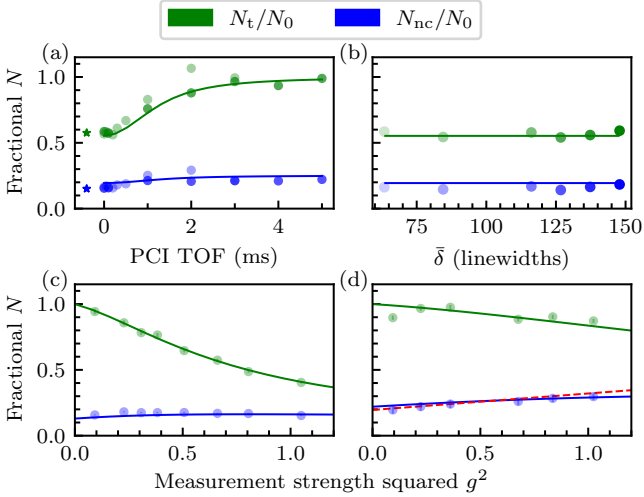


FIG. 2. Photoassociation losses. Fractional total number of atoms (green) and number of atoms outside the BEC but within a 1 recoil momentum circle (blue) following measurement. The symbols mark experimental data while the curves are the result of our 2-body PA model. In all cases, the opacity of the points reflects the detuning. (a) Short TOF varied dispersive measurements at two different probe detunings ($\delta = -84.5$ and $\delta = -126.7$). All measurements were at measurement strength $g \approx 1$, which was attained by adjusting intensity to $\bar{I} \approx 9.5$ and $\bar{I} \approx 21$ respectively. Star symbols mark *in situ* measurements with the ODT on (plotted at negative TOF for display purposes). (b) *In situ* measurements at different $\bar{\delta}$ all with $g \approx 1$. Measurement time was $t_m = 25 \mu s$ in (a) and (b). (c) and (d) Loss as a function of g^2 both *in situ* in (c) and with a 2 ms TOF in (d). The red dashed line in (d) plots the expected $g^2/8$ light-scattering behavior. Both cases were at $\bar{\delta} = -84.5$ and $\bar{I} \approx 9.5$ with t_m varied from 4 μs to 36 μs .

B. Photoassociation

We used the post-measurement atom number as a preliminary probe of measurement back-action and found that at our high *in situ* atomic densities of $1 \times 10^{14} \text{ cm}^{-3}$, photoassociation (PA) leads to rampant atom loss [15]. Although PA is suppressed at blue detuning, we demonstrate the importance of these losses by preparing BECs with N_0 total atoms in $|g_2\rangle$ and measuring fractional change in total atom number N_t/N_0 and in uncondensed number N_{nc}/N_0 [28]. N_{nc}/N_0 counts both thermal atoms as well as atoms that have undergone large-angle light scattering.

Fig. 2(a) confirms that this is a 2-body process by reducing the atomic density with a short TOF. We find that the losses rapidly drop starting at $t_{\text{TOF}} \approx 0.5$ ms (when mean-field driven expansion becomes significant) and vanish after 3 ms (at which time the density has dropped by a factor of nearly 20). We also investigated another potential loss mechanism due to two-color PA resulting from the combination of the intense dipole trapping beam and the probe beam. Data taken just before (star symbols at negative time for clarity) and just after

the ODT turn-off have no difference in loss, confirming the absence of any two-color PA effects.

Panel (b), taken *in situ*, shows that the fractional number is independent of $\bar{\delta}$. These data were taken at constant P_e (achieved by tuning \bar{I}) and demonstrate that there are no PA resonances. Figure 2(c) shows that *in situ* the total number drops rapidly with increasing g^2 while the number outside the BEC remains constant. This verifies that the high-density BEC undergoes PA while the low density thermal cloud is left mostly unchanged. Lastly Fig. 2(d) plots these quantities following a 2 ms TOF, confirming the same reduced losses found in (a). Furthermore N_{nc} increases linearly with slope $g^2/8$ (red dashed curve) as expected from photon scattering.

Our data is well described by a 2-body loss model (solid curves), however, these simulations require a 2-body loss coefficient that is in excess of previous measurements [29] by a factor of about 20. Lastly, we note that light traversing the BEC acquires a phase shift causing the atomic cloud to act as a lens. When the phase shift is in excess of about 1 radian the scattering is no longer described by our model and atomic cloud experiences excess compression, potentially enhancing 3-body loss. The absence of $\bar{\delta}$ dependence in Fig. 2(b) affirms that effects such as this arising from the ac Stark shift do not contribute to loss.

III. DETECTING WAVEFUNCTION CHANGE VIA RAMSEY INTERFEROMETRY

Here we characterize the light matter interaction, as well as back-action, predicted by our quantum trajectories model using Ramsey interferometry (RI). Our Ramsey interferometer [Fig. 3(a,b)] commenced with a resonant microwave pulse driving a $\pi/2$ rotation about \mathbf{e}_y , taking the atoms from $-\mathbf{e}_z$ (in $|g_1\rangle$) to \mathbf{e}_x . Then during the free evolution time we applied the probe laser detuned by $\bar{\delta}$ from the $|g_2\rangle$ to $|e\rangle$ transition for a time t_m ; the resulting ac Stark shift drove a rotation about \mathbf{e}_z by ϕ (solid red arc). A second microwave pulse drove a $\pi/2$ rotation about an axis rotated by $\delta\phi_P$ at which time we measured the final populations N_1 and N_2 in $|g_1\rangle$ and $|g_2\rangle$ respectively in TOF, giving the fraction in $|g_2\rangle$ as $R_2 = N_2/(N_1 + N_2)$. The black data in Fig. 3(c), taken with the probe laser off, shows that the resulting fractional population R_2 is sinusoidal, and the red data, with the probe on, is phase shifted (from the ac Stark shift on $|g_2\rangle$). We obtain the phase shift ϕ , contrast A , and center shift b with fits to $R_2 = [1 + A \cos(\delta\phi_P + \phi)]/2 + b$.

The RI phase shift is a direct measure of the differential phase acquired during free evolution, here $-V_{\text{ac}}t_m/h$ from the ac Stark shift of $|g_2\rangle$ due to the probe beam [30], with $V_{\text{ac}} = \Gamma\bar{I}/(8\bar{\delta})$. The data in Fig. 3(d) was taken at $\bar{\delta} = 63.4$ and 116.2 (red and green respectively). As expected the slope is larger for smaller $\bar{\delta}$, but in both cases the acquired phase can exceed 2π at which point it wraps back to zero. The intensity of the probe laser is difficult to obtain in-vacuo [31, 32]; however, fitting $t_m V_{\text{ac}}$ to these

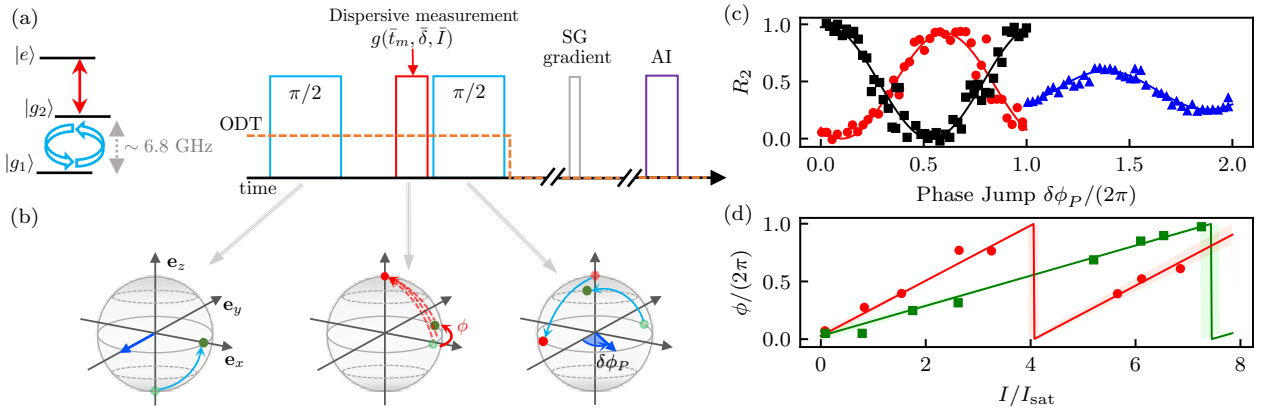


FIG. 3. Ramsey interferometry. (a) Level diagram (left) and time sequence (right) for RI. An initial $\pi/2$ microwave pulse (light blue) is followed by a 15 μ s evolution period; then the $t_m = 20 \mu$ s off-resonant light pulse (red) is applied, and after a 5 μ s delay (giving a total $T = 40 \mu$ s free evolution time) the Ramsey sequence is completed with a second $\pi/2$ pulse (light blue). The ODT (orange dashed) is extinguished immediately following the Ramsey sequence. A Stern-Gerlach (SG) gradient (grey) during the 20 ms TOF spatially separates states $|g_1\rangle$ and $|g_2\rangle$, which are then detected using standard absorption imaging (AI, purple). (b) Bloch sphere depiction of RI. The dark blue arrows depict the axes of rotation for each microwave pulse and the light blue arrows mark the associated trajectories. The green circles show the coherent evolution during each step of our sequence. Red arrows depict evolution associated with the measurement pulse with the solid curve resulting from the Stark shift and dashed curves resulting from measurement back-action. The red circles are the states that were measured to be in $|g_2\rangle$. Translucent(solid) symbols indicate the initial(final) states. (c) Ramsey oscillation without (black) and with the light pulse at $\bar{\delta} = -63.4$ and $\bar{I} \approx 2$ (red) and $\bar{I} \approx 7$ (blue), taken *in situ* as the phase jump $\delta\phi_P$ between the two pulses is varied. Solid curves are fits to the equation given in the text. Blue Ramsey data $\delta\phi_P$ values are deliberately shifted by 2π to visualize the reduction in contrast and the larger phase shift. (d) Optically induced phase shift ϕ as a function \bar{I} at $\bar{\delta} = -63.4$ (red) and $\bar{\delta} = -116.2$ (green). The same-color lines are fits to $-V_{\text{ac}}t_m/\hbar \bmod 2\pi$. Shaded regions indicate the $\pm 1\sigma$ statistical uncertainty range.

data gives a primary calibration of the laser intensity [33], providing a conversion between our camera signal [34] and I_{sat} with $< 5\%$ fractional uncertainty. The solid lines in Fig. 3(c) are the result of this fitting process.

Figure 3(c) shows a second effect of increasing measurement strength (blue data): the Ramsey contrast decreases with increasing g , implying that the post-measurement many-body wave function is not described by a coherent superposition of $|g_1\rangle$ and $|g_2\rangle$.

Our measurement model predicts this effect: as illustrated in the middle Bloch sphere in Fig. 3(b), each time a photon is spontaneously scattered and detected by the environment, the wavefunction of a single atom collapses into $|g_2\rangle$ (along \mathbf{e}_z), losing any coherence with $|g_1\rangle$ (red dashed arrows). The second $\pi/2$ pulse always returns that atom to the equator of the Bloch sphere, reducing the contrast by $1/N$. In this situation, the per-atom probability of scattering a single photon at large angle is $g^2/16$ (see App. C for the complete calculation). By contrast for collective scattering (generally at small-angle), a detected photon was scattered off of the global density distribution yielding Mössbauer-like collective back-action and no reduction in contrast. As a result, the change in contrast measures the number of spontaneously scattered photons [35].

Our RI observations summarized in Fig. 4(b) are wildly inconsistent with the theoretical prediction. In the following sections we systematically identify and eliminate the factors leading to this disagreement, and thereby en-

ter a regime where true quantum back-action limited measurements of BECs are possible.

A. Spin-echo

Spatial inhomogeneities in the probe beam as well as near-dc magnetic field noise can reduce the RI contrast. In the first case, the resulting position-dependent ac Stark shift imprints spatial structure to the RI phase ϕ , thereby reducing the spatially averaged contrast. Second, because the $|g_1\rangle$ - $|g_2\rangle$ transition is first-order sensitive to the external magnetic field, the RI contrast is reduced when field noise randomly shifts the resonance condition between different repetitions of the experiment.

We added a spin-echo pulse to our interferometer [see Fig. 4(c)-left] to compensate for both of these parasitic effects. As Fig. 4(a) shows, the noise in the spin-echo signal (green) is reduced compared to the standard RI measurement (blue). Although the measurement noise is reduced, the contrast with spin echo is unchanged, leaving the substantial disagreement with our theory prediction (black curve) due to the systematic factors we report next.

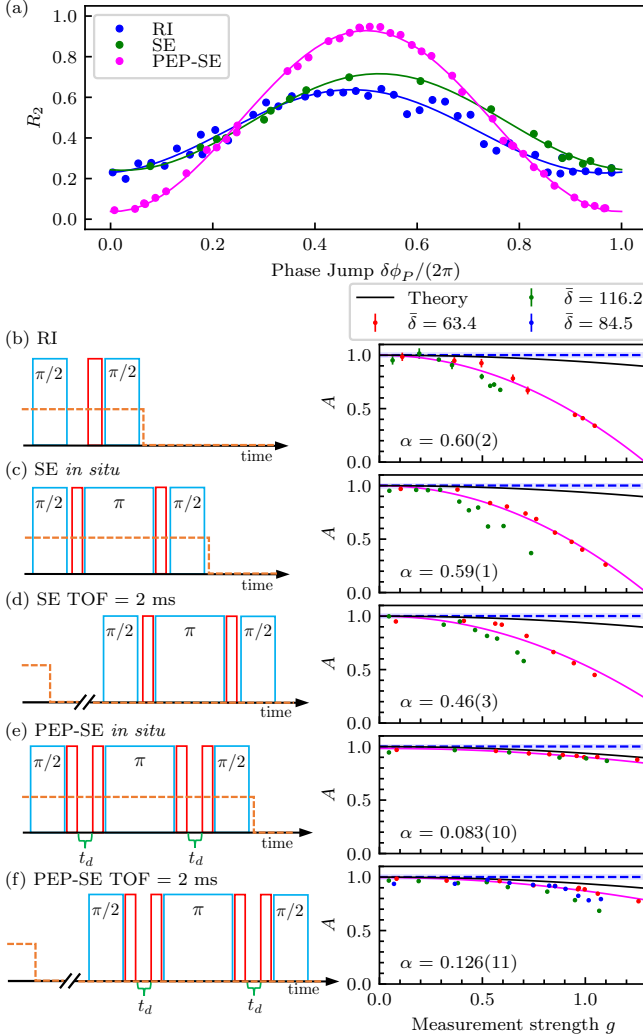


FIG. 4. Ramsey interferometer contrast. (a) Ramsey fringes measured using Ramsey interferometry (blue), spin-echo (SE, green) and pulse-evolve-pulse with spin-echo (magenta) sequences. All measurements were performed *in situ* at $\bar{\delta} = -63.4$ with $\bar{I} \approx 7$ yielding $g \approx 1$. (b)-(f) Dependence of contrast A on g (right) for different pulse schemes (left). In the pulse schemes, the dashed orange lines denote the intensity of the ODT, the red blocks are the dispersive measurement pulses, and blue bars are the microwave pulses. (b) *In situ* RI measurements. (c) *In situ* RI with spin-echo measurements. (d) Spin-echo after 2 ms TOF measurements. (e) *In situ* PEP-SE measurements. (f) PEP-SE sequence after 2 ms TOF measurements. The horizontal blue lines show the RI contrast observed without the measurement pulse. The black curves plot the prediction of our model. The pink curves depict a fit of the $\bar{\delta} = 63.4$ data to $A = A_0 - \alpha g^2$.

B. Time of flight

As detailed in Sec. II B, PA induced by the probe beam precipitates atom loss. To study the impact of PA loss on RI contrast, we added a short TOF to the spin-echo sequence as shown in Fig. 4(d)-left, simultaneously reducing the atomic density and accounting for position de-

pendent ac Stark shift effects [Sec. III A]. The RI contrast presented in Fig. 4(d)-right increased by $\approx 25\%$ as compared to the *in situ* RI and spin-echo data in Fig. 4(b,c) respectively. Nonetheless, the observed RI contrast still differs significantly from the predicted value, ultimately resulting from the third systematic effect, the stray weak lattice studied below.

C. Stray lattice

Contrary to our predictions, Figs. 4(b)-(d) show that the contrast depends on probe detuning (green versus red data). This difference signifies the presence of the third parasitic effect: a weak optical lattice generated by the probe beam interfering with its retro-reflections off subsequent optical elements [36].

As a result, each probe pulse corresponds to the sudden application of a lattice potential. Weak lattices create populations in matterwave diffraction orders with momentum $\pm 2\hbar k_0$. In principle a suitable spin-echo sequence could remedy this, nonetheless, the rapidly moving diffracted atoms experience different lattice potentials during our first and second pulses precluding effective cancellation.

Instead we extended the ideas in Refs. [37, 38] by splitting each probe pulse into two pulses of duration $t_p = 8.2 \mu\text{s}$ spaced in time by a carefully chosen $t_d = 25.6 \mu\text{s}$ of free evolution, essentially unwinding the phase imprinted by the lattice (see App. E). The left panel of Fig. 4(e) shows such a pulse-evolve-pulse with spin-echo (PEP-SE) sequence. The near-full contrast magenta Ramsey fringe in Fig. 4(a) results from this PEP-SE sequence applied *in-situ* for $g \approx 1$, and indeed the data in Fig. 4(e)-right converge to the expected contrast.

This is surprising given that the pulse sequence was applied *in situ* causing the BEC to suffer from PA induced atom loss. We therefore added a 2 ms TOF prior to this pulse sequence to mitigate the PA losses [Fig. 4(f)-left]. As shown in Fig. 4(f)-right, we observed a modest *reduction* in contrast, and as with (b)-(d), data taken at larger detuning are impacted more significantly. We attribute this reduction to the changing optical intensity profile that the falling BEC experiences as it traverses different regions of the probe during the pulse sequence; this compromises both the spin echo and our PEP-SE scheme.

D. Further considerations

Even though RI contrast is a direct measure of the overall wavefunction change, these data show that RI contrast alone is insufficient to identify back-action dominated measurement regimes. Thus to verify that a measurement could be—even in principle—back-action limited it is essential to separately quantify decoherence and

atom loss as we do in this paper. The reduction in RI contrast with the measurement pulse sequence applied after a short TOF highlights an interesting interplay between distinct systematic effects. Still, most real applications weak measurements would be performed *in-situ*, making the limitations of measurements performed after a short TOF irrelevant. The more essential challenge, discussed further in Sec. V, is to reduce the *in-situ* PA loss rate.

IV. MEASUREMENT INDUCED HEATING: THE GOOD, THE BAD AND THE UGLY

The back-action resulting from measuring the reservoir invariably adds energy to the system as $|\Psi_S\rangle \rightarrow |\Psi'_S\rangle$. The added energy is an extensive quantity resulting from the change in $|\Psi'_S\rangle$ with contributions both from kinetic and interaction energies. In BECs, the added interaction energy derives from the change in density as outgoing scattered atoms interfere with the BEC mode. We obtain the total energy E_t bolometrically by measuring the temperature T following thermalization, and contrast the cases of a BEC and a thermal gas.

Evaporative processes can reduce the temperature by removing atoms from the trap, making bolometry ineffective. To mitigate this effect we increased the trap depth [leading to harmonic trap frequencies $(\omega_x, \omega_y, \omega_z) = 2\pi \times [22.6(3), 337(2), 265(2)]$ Hz]. We then applied the dispersive measurement, i.e., the far-detuned probe laser pulse, allowed the system to thermalize for 400 ms, and extracted the final temperature from TOF images obtained via resonant absorption imaging.

Our TOF data generally consisted of bimodal density distributions with contributions from condensed and uncondensed atoms. We obtain T as well as N_c and N_{nc} following the approach in Refs. [39, 40] (see App. F 1). Figure 5(a) shows the observed total number $N_t = N_c + N_{nc}$ from this procedure as a function of $\bar{\delta}$ for two measurement times t_m . The variation in number for large $\bar{\delta}$ derives from long-term drift in our apparatus. These data show that for sufficiently small detuning N_t begins to decrease from PA losses. We therefore treat N_t as a gate marking data for which bolometry is valid; the curves depict exponential fits and we accepted data when the curve exceeds 85 % of its maximum value (unshaded regions). In the following figures data rejected by this threshold are plotted as hollow symbols.

The condensate fraction $R_c = N_c/N_t$ and temperature T shown in Fig. 5(b) and (c) consistently indicate that increasing the measurement strength parameter g —either from reducing $\bar{\delta}$ or increasing t_m —are increasingly destructive, increasing T and reducing R_c in tandem. As described in App. F 2, the condensate fraction in (b) in conjunction with the temperature in (c) allow us to extract the BEC transition temperature $T_c = 165$ nK for our $N \approx 10^5$ atom system [horizontal magenta dotted lines in (c) and (f)], which is reduced with respect to the 3D non-interacting value of $T_c^0 = 225$ nK for a harmon-

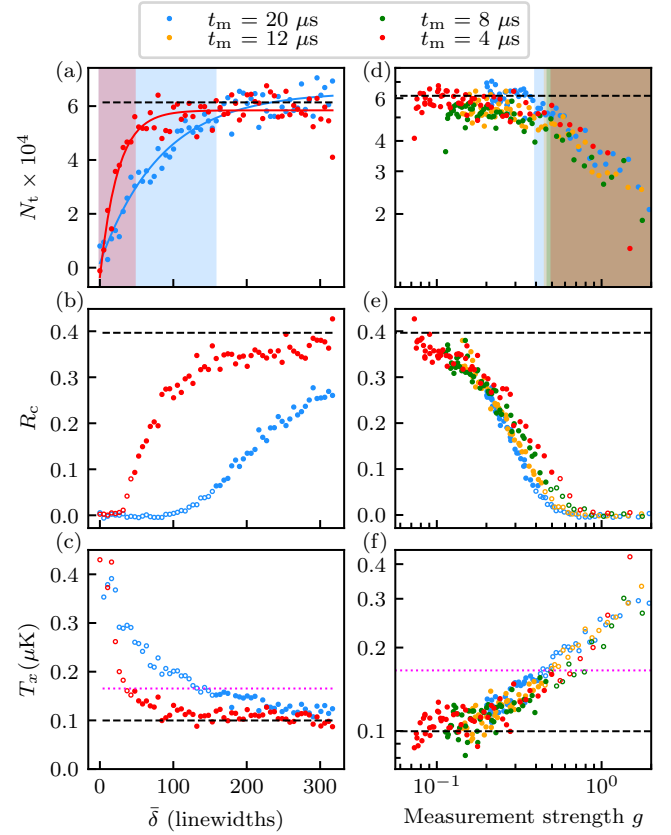


FIG. 5. Measurement induced heating of a BEC. Left: Results for measurement times $t_m = 4 \mu\text{s}$ and $20 \mu\text{s}$ plotted as a function of $\bar{\delta}$. Right: Data plotted as a function of g on logarithmic scale, with data excluded as described in the text plotted with hollow symbols. (a), (d) Total number N_t . The solid curves in (a) are fits to a rising exponential function and the shaded regions are where N_t has fallen below 85 % of its asymptotic value. (b), (e) Condensate fraction R_c . (c), (f) Temperature T . The magenta dashed line marks the condensation temperature T_c . The dashed black lines depict the results where no weak measurement was performed. Each data point is the average of 5 iterations of the experiment.

ically trapped gas. This suppression primarily results from our system being transitional from 3D to 1D with μ only about 3 times larger than the transverse trap frequencies.

Panels (d)-(f) expand on this observation by plotting such data taken for four values of t_m as a function of g and show all of our observations nominally collapse onto the same curve. In the limit of small changes in N_t , PA losses are proportional to g^2 , but would lead to little change in T (see below).

As a reference case we also measured the change in temperature of a dilute thermal gas at $T/T_c \approx 2.5$. The observed N_t and T results for different measurement times for the thermal gas case are presented in Appendix F 3. In this case the energy [Fig. 6(a)] is well approximated by the ideal gas result $E_t = 3Nk_B T$ in a harmonic trap with Boltzmann constant k_B . The magenta curve plots the expected increase in temperature

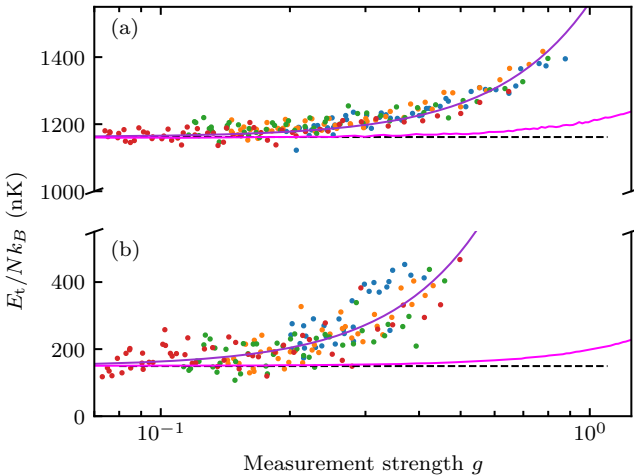


FIG. 6. Added per-atom energy for a range of measurement times for both (a) a thermal gas and (b) a BEC. In both cases the magenta curve plots the predicted added kinetic energy obtained from numerically evaluating increase in kinetic energy. The purple curves are fits to $E = E_0 + \beta g^2$ and the black dashed lines depict the initial energy. The color-scale for the data is the same as in Fig. 5.

$\delta E = E_0 + \beta g^2$ (with $\beta = 54.9(3)$ nK) for large angle scattering, i.e., spontaneous emission while the solid purple curve is a fit to the expected functional form yielding $\beta = 400(10)$ nK, a factor of 7 larger than can be explained by light scattering alone.

For a weakly interacting BEC the per-particle energy [25] is

$$\frac{E_t}{Nk_B T_c^0} = \frac{3\zeta(4)}{\zeta(3)} \bar{T}^4 + \frac{1}{7} \bar{\mu} (1 - \bar{T}^3)^{2/5} (5 + 16\bar{T}^3), \quad (6)$$

in terms of $\bar{T} = T/T_c^0$, $\bar{\mu} = \mu/(k_B T_c^0)$, and the Riemann zeta function $\zeta(x)$ (see App. F 2). This allows us to obtain E_t below T_c as plotted in Fig. 6(b). As with the thermal gas case, the added energy E_t is far in excess of the kinetic energy added by spontaneous emission (magenta curve), which gives $\beta = 54.9(3)$ nK [41] as compared to the fit value $\beta = 1310(80)$ nK.

Both of these observations are consistent with the stray optical lattice detailed in Sec. III C, indicating that the per-atom energy is dominated by the contributions from the lattice. Our pulse-evolve-pulse scheme is only effective for momenta near zero, thereby rendering it ineffective for measurements at higher temperature. These include data from the thermal cloud as well as the BEC in the deep trap, for which $R_c \approx 0.4$.

For this reason, we made measurements with the pulse-evolve-pulse sequence at reduced temperature (with $T = 41$ nK and $R_c \approx 0.77$). We reduced the temperature by first starting with a colder BEC and then increasing the trap depth only $\approx 2 \times E_0$ (a factor of ≈ 2.3 shallower than the data discussed above), where $E_0 = \hbar^2 k_0^2 / (2m)$ is the single photon recoil energy with recoil momentum k_0 . This gives reduced heating due to compression, and is still sufficient to trap scattered atoms. Subsequently

we applied the pulse-evolve-pulse measurement scheme and varied $\bar{\delta}$ at three different probe intensities I keeping t_m constant. We find that the added energy E_t is decreased by half compared to the single pulse measurements, giving $\beta = 725(17)$. While this is a marked improvement it is still more than ten times in excess of the simple spontaneous emission prediction. Given the notorious difficulty of measuring the temperature of deeply degenerate BECs [42], it is likely that our temperature measurements overestimate the true temperature. In addition, we do not account for any energy imparted by probe inhomogeneities.

The PA process described in Sec. II B adds energy by preferentially removing atoms from regions of high density. In a harmonic trap the high-density regions are those with the lowest potential energy. As a consequence, this loss process increases the per-particle energy of the remnant atoms: anti-evaporation. We numerically simulated this process and found that it was not a significant contributor. In the case of a thermal gas, we numerically find that a 2-body PA loss model increases the per-particle energy by a maximum of 15 % for the data presented in Fig. 6.

V. CONCLUSION AND OUTLOOK

Most quantum technologies simultaneously require quantum limited measurements and real-time control. To this end, back-action limited measurements of ultracold gases are essential for fully realizing this system's potential. For example, the interplay between measurement back-action and the actual information extracted from the system limits feedback cooling of atomic gases [43–45]. In addition to simply cooling into established quantum states (both weakly and strongly correlated), closed-loop feedback enables the engineering of artificial, non-local, and non-Markovian, reservoirs. Known examples using feedback include spin squeezed states [46] and new Mott insulators [47]; and existing proposals with engineered reservoirs show that suitable quantum jumps can equilibrate into strongly correlated states [48].

Here, we presented initial experiments mitigating systematic effects that otherwise prevent back-action limited measurements. In our experiment, data taken with $g \lesssim 0.3$ (with per-atom spontaneous scattering probability $P_{sp} \lesssim 0.01$, see App. B for a brief discussion of the implications to the SNR) had no discernible loss in Ramsey contrast, no detectable heating, and minimal atom loss: functionally non-destructive [16]. However, our results demonstrate that such functionally non-destructive measurements can be far from quantum back-action limited. This result is a step on the path to closed-loop control of quantum gases.

For our *in situ* results—with rampant PA losses—photon scattering from the measurement process does not fully explain the change of the system's state. Consequently such measurements are not back-action limited,

even in principle. For the modest range of detuning explored here, the PA loss rate scales as the excited state probability $P_e \propto g^2$; this implies that for a target measurement strength, PA losses are not reduced until vastly larger detuning when this scaling breaks down [49]. As a consequence, back-action limited measurements of BECs can be achieved either by managing the atom density, or by careful management of molecular resonances [50]. In degenerate Fermi gases the Pauli pressure leads to much lower densities [51], typically an order of magnitude or more dilute than BECs, making PA losses less significant.

The probe beam was inhomogeneous and additionally gave rise to an optical lattice from stray reflections. The impact of large scale inhomogeneities—typically from forward scattered light from dust and other imperfections in the imaging system—can be mitigated with a traditional spin-echo sequence, and we find that these did not significantly reduce the contrast. But matterwave diffraction from stray optical lattices lead to atomic motion on the time scale of our pulse sequence and as such the spin-echo sequence was insufficient to compensate for this effect. Rather we demonstrated an echo-like pulse sequence of the probe beam that nulled matterwave diffraction for atoms initially moving slow compared to the recoil velocity.

The 4π steradian measurement model we developed is powerful and makes reliable predictions. While a convenient theoretical abstraction, this model does not derive from a practical experimental measurement geometry. The use of optical cavities to control the mode structure of light provides one way to overcome this limitation, enabling back-action limited measurements [52–54] of systems coupled to just a handful of optical modes.

The second-order light matter interaction in Eq. (1) is $\propto 1/\delta$ and purely dispersive in the classical limits: when $\hat{E} \rightarrow \langle \hat{E} \rangle$ the atoms experience only an AC Stark shift, and when $\hat{n}_g \rightarrow \langle \hat{n}_g \rangle$ the light experiences only a phase shift. Despite this, Eq. (1) accounts for both spontaneous and stimulated emission with their $\propto 1/\delta^2$ and $\propto 1/\delta$ scaling respectively. This gives both the imaginary (dissipative) and real (dispersive) parts of the atomic susceptibility. There are multiple measurement techniques for quantum gases based on the dispersive light-matter interaction [16, 19, 39, 55] that in principle can give back-action limited measurement outcomes. In particular, we use digitally enhanced PCI [20], an optical homodyne detection technique that accounts for imaging system imperfections.

Employing the strategies identified here is necessary to enable back-action limited measurements, but after leaving the atomic ensemble the scattered light must actually be detected. Fundamentally this requires an imaging system with minimal losses and large numerical aperture in conjunction with a high efficiency detector, as any scattered light that is not detected is effectively measured by the environment and its information is lost. Furthermore, the captured signal must lead to a faithful representation of the atomic ensemble, necessitating an imaging system

with minimal or well calibrated aberrations as we demonstrated in Ref. [20]. Lastly, the initial optical field must be well known, for which techniques such as the RI outlined here and described in more detail in Ref. [33], are essential. These physical considerations do not touch on technical matters such as calibrating the response and hardware specific noise properties of the physical detector, i.e., a charge coupled device (CCD) or complementary metal oxide semiconductor (CMOS) camera. Future work needs to account for these sources of technical noise.

Backaction limited weak measurements enable new probes of quantum systems and offer new ways to understand the measurement process. For example, the decomposition of the Kraus operators into separate average density and fluctuation terms provides a clear real-space picture explaining the suppression of spontaneous emission from systems with reduced density fluctuations. These include not only degenerate Fermi gases [12–14], but Mott insulators of either fermions or bosons [56, 57].

A weak measurement of strength g can be also decomposed into a series of N sub-measurements [58, 59] each with strength g/\sqrt{N} . In this configuration, the total outcome of these measurements recovers an individual measurement of strength g , but the quantum back-action of earlier measurements correlates with the outcome of later measurements, giving information that is erased in a single stronger measurement.

ACKNOWLEDGMENTS

The authors thank J. V. Porto and M. Gullans for carefully reading the manuscript. This work was partially supported by the National Institute of Standards and Technology, and the National Science Foundation through the Physics Frontier Center at the Joint Quantum Institute (PHY-1430094) and the Quantum Leap Challenge Institute for Robust Quantum Simulation (OMA-2120757).

Appendix A: Linking quantum trajectories to conventional parameters

Here we outline the relationships between conventional experimental parameters and the relatively abstract quantities employed in deriving the coupling strength $g_\sigma(\mathbf{k}_\perp)$ in Eq. (3).

We establish these relationships starting with the photon field operator expectation value α_0 and relate it to the optical intensity I :

$$I = \frac{1}{2} \epsilon_0 c |E|^2 = \hbar \omega_{\text{ge}} c |\alpha_0|^2. \quad (\text{A1})$$

In the second statement we inserted the expression

$$|E|^2 = \frac{2\hbar\omega_{\text{ge}} |\alpha_0|^2}{\epsilon_0} \quad (\text{A2})$$

for the magnitude of the electric field. The saturation intensity is a key metric of the light-matter interaction; for arbitrary light polarization

$$I_{\text{sat}} = \frac{\epsilon_0 c \Gamma^2 \hbar^2}{4|\epsilon_{\sigma_0}(\mathbf{k}_0) \cdot \mathbf{d}_{\text{ge}}|^2}. \quad (\text{A3})$$

As detailed in Sec. I, \mathbf{d}_{ge} is the dipole matrix element for transitions between ground and excited state atoms with energy difference $\hbar\omega_{\text{ge}}$ and $\epsilon_{\sigma}(\mathbf{k}_0)$ are the polarization vectors as pairs of orthogonal vectors transverse to \mathbf{k}_0 . In terms of these parameters the transition linewidth is

$$\Gamma = \left(\frac{|\mathbf{k}_0|^3}{3\pi\hbar\epsilon_0} \right) |\mathbf{d}_{\text{ge}}|^2. \quad (\text{A4})$$

We recall the standard definition for saturation intensity

$$\frac{I}{I_{\text{sat}}} = 2 \left| \frac{\Omega}{\Gamma} \right|^2, \quad (\text{A5})$$

acquired from a more traditional treatment, where

$$\Omega = |\epsilon_{\sigma_0}(\mathbf{k}_0) \cdot \mathbf{d}_{\text{ge}}| \frac{E_0}{\hbar} \quad (\text{A6})$$

is the Rabi frequency. We next express Ω in terms of the coupling strength and the optical field amplitude α_0 giving

$$\Omega = 2|g_{\sigma_0}(\mathbf{k}_0)\alpha_0|. \quad (\text{A7})$$

These relations allow us to bridge between conventional laboratory parameters and the theoretical parameters employed in our model. For example, we combine Eq. (A1) and Eq. (A3), to obtain

$$\bar{I} = \frac{I}{I_{\text{sat}}} = \frac{8|\alpha_0 g_{\sigma_0}(\mathbf{k}_0)|^2}{\Gamma^2} \quad (\text{A8})$$

in agreement with Eq. (A5) and Eq. (A7).

We now turn to the scattering probability $P_{\text{sp}} = \Gamma t_{\text{m}} P_{\text{e}}$ (introduced in Sec. IA), which contains the excited state probability

$$P_{\text{e}} = \frac{|\alpha_0 g_{\sigma}(\mathbf{k}_0)|^2}{\Delta^2}. \quad (\text{A9})$$

This, along with Eq. (A8), allows us to rewrite the scattering probability as

$$P_{\text{sp}} = |\alpha_0 g_{\sigma_0}(\mathbf{k}_0)|^2 \frac{\Gamma t_{\text{m}}}{\Delta^2} = \frac{\Gamma t_{\text{m}}}{8} \frac{I}{I_{\text{sat}}} \frac{\Gamma^2}{\Delta^2}. \quad (\text{A10})$$

This expression is organized into the physically relevant dimensionless quantities \bar{t}_{m} , \bar{I} and $\bar{\delta}$ introduced in the main text. In Sec. IA, we defined the overall measurement strength using these parameters and made the choice to not include the factor of 8 so

$$g^2 = \frac{I}{I_{\text{sat}}} \frac{\Gamma t_{\text{m}}}{(\Delta/\Gamma)^2} = 8P_{\text{sp}}. \quad (\text{A11})$$

As such, a measurement strength of $g^2 = 1$ signifies a probability of 1/8 for an atom to scatter a single photon at large angle.

Appendix B: Measurement strength and signal to noise

Here we briefly consider the relation of g to SNR for the determination of atom number using either forward-directed collectively scattered light or spontaneously scattered light. For standard imaging, directly detecting the collectively scattered light would typically be performed using dark-field imaging (which in principle has the same SNR as PCI), and detecting the spontaneously scattered light would be realized via fluorescence imaging. In principle there is no hard distinction between these techniques since large numerical aperture imaging systems can capture significant contributions from both. For practical experiments with degenerate gases the forward scattered light dominates.

For a BEC, and for simplicity assuming an isotropic (rather than dipole) scattering distribution, the scattering probabilities are

$$P_{\text{tot}} = P_{\text{col}} + P_{\text{sp}} \propto N^2 G + \frac{k_0^2 N}{\pi}, \quad (\text{B1})$$

where

$$G = \oint \frac{d^2 \mathbf{k}_{\perp}}{(2\pi)^2} |n_{\mathcal{F}}(\mathbf{k}_0 - \mathbf{k}_{\perp})|^2 \sim \frac{1}{A} \quad (\text{B2})$$

is a geometric factor and A is the cross-sectional area of the system normal to the imaging axis (in detail this depends on the exact density distribution). Thus the ratio of collective to spontaneous scattering is $\sim \pi N/(k_0^2 A)$ and the total number of spontaneously and collectively scattered photons is

$$N_{\text{sp}} = N \frac{g^2}{8}, \quad \text{and} \quad N_{\text{col}} = \frac{\pi N^2 G}{k_0^2} \frac{g^2}{8}. \quad (\text{B3})$$

For our system with $N \approx 7 \times 10^4$ and transverse TF radii $(R_x, R_y) \approx (43, 4) \mu\text{m}$ the ratio of these is ≈ 6 .

The integrated number of spontaneously scattered photons gives an SNR of $g\sqrt{N/8}$ for the determination of the atom number N . For example, for our BEC and $g = 0.3$ about $N_{\text{sp}} = 800$ photons would be spontaneously scattered. This implies that the forward scattered light would contain about $N_{\text{col}} = 5 \times 10^3$ photons.

In both cases the uncertainty in the photon number is simply the square root of the photon number. The SNR in the atom number derived from spontaneously scattered light is therefore ≈ 30 since the atom number is proportional to N_{sp} . For the forward scattered light, the atom number is proportional to $N_{\text{col}}^{1/2}$ giving a SNR of ≈ 140 . In both cases the SNR is proportional to g .

Appendix C: Ramsey Interferometry with Measurement Induced Decoherence

We consider two-states $\{|g_1\rangle \equiv |\downarrow\rangle, |g_2\rangle \equiv |\uparrow\rangle\}$ that are microwave coupled with the rotating wave Hamiltonian

$$\hat{H}'(\phi_P) = \frac{1}{2} [\Delta \hat{\sigma}_z + \Omega_\mu \sin(\phi_P) \hat{\sigma}_x - \Omega_\mu \cos(\phi_P) \hat{\sigma}_y],$$

in terms of the detuning Δ (in this case $\Delta > 0$ corresponds to red detuning and $\Delta < 0$ yields blue detuning, this reversed with respect to the spectroscopy convention), coupling strength Ω_μ and microwave oscillator phase ϕ_P .

1. Standard RI

We first outline the basic framework describing Ramsey interferometry for an arbitrary many-body state. Consider an atomic ensemble in an initial state $|\Psi_i\rangle$ along $-\mathbf{e}_z$ on the Bloch sphere (with no population in $|\uparrow\rangle$), i.e., $\hat{b}_\uparrow |\Psi_i\rangle = 0$.

In the second quantized notation, the operator

$$\hat{R}_z(\theta) \equiv \exp \left[i \frac{\theta}{2} \hat{b}_i^\dagger \sigma_{z,ij} \hat{b}_j \right] = \exp \left[i \frac{\theta}{2} \left(\hat{b}_\uparrow^\dagger \hat{b}_\uparrow - \hat{b}_\downarrow^\dagger \hat{b}_\downarrow \right) \right],$$

implements a spin-rotation about \mathbf{e}_z by the angle θ , and similarly for the other two axes (note that we used an implied summation convention in this expression). Here $\sigma_{x,y,z}$ is the Pauli matrix for the specified axis. Our experimental sequence began with a $\pi/2$ pulse to rotate the system into the equal superposition state $(|\uparrow\rangle + |\downarrow\rangle)/\sqrt{2}$, aligned along \mathbf{e}_x on the Bloch sphere.

The RI completed with a second $\pi/2$ pulse, that drove rotations about the $\mathbf{e}_x \sin \delta\phi_P - \mathbf{e}_y \cos \delta\phi_P$ axis (implemented by phase shifting the microwave oscillator by $\delta\phi_P$). The final state is

$$|\Psi_f\rangle = \left[\hat{R}_z^\dagger(\delta\phi_P) \hat{R}_y(\pi/2) \hat{R}_z(\delta\phi_P) \right] \hat{R}_y(\pi/2) |\Psi_i\rangle, \quad (\text{C1})$$

We are interested in both the probability of detecting scattered photons and the change in RI contrast. As before, we assume all atoms are initially in $|\downarrow\rangle$ number state. We begin with the scattering probability $P(\mathbf{k}_f)$ giving

$$\begin{aligned} P(\mathbf{k}_\perp) &= \langle N | \hat{R}_y^\dagger(\pi/2) \hat{R}_z^\dagger(\delta\phi_P) \hat{M}^\dagger(\mathbf{k}_\perp) \hat{R}_y^\dagger(\pi/2) \hat{R}_y(\pi/2) \hat{M}(\mathbf{k}_\perp) \hat{R}_z(\delta\phi_P) \hat{R}_y(\pi/2) | N \rangle \\ &= \frac{t_m P_e}{c} |g(\mathbf{k}_\perp)|^2 \frac{N}{2} \left[\frac{N-1}{2} \left| \int \frac{d^3 \mathbf{k}_1}{(2\pi)^3} \tilde{\psi}_\downarrow^*(\mathbf{k}_1) \tilde{\psi}_\downarrow[\mathbf{k}_1 - (\mathbf{k}_\perp - \mathbf{k}_0)] \right|^2 + 1 \right]. \end{aligned} \quad (\text{C4})$$

This reproduces Eq. (5) but with atom number N essentially reduced by $1/2$ (owing to the $\pi/2$ pulse prior to applying the measurement pulse). As elaborated on in the main text, the first term describes collective (stimulated) scattering with integrated probability $P_{\text{col}} \propto N^2$ whereas the second term stems from spontaneous emission with probability $P_{\text{sp}} \propto N$.

where the quantity in square brackets implements the rotation about the new axis. In this standard RI scheme, for the initial state with all atoms in $|\downarrow\rangle$ the number of atoms in state $|\uparrow\rangle$ in the final state is

$$\langle \hat{n}_\uparrow \rangle = \langle \Psi_f | \hat{b}_\uparrow^\dagger \hat{b}_\uparrow | \Psi_f \rangle = N \cos^2(\delta\phi_P/2). \quad (\text{C2})$$

Here, the total number of atoms N in the initial state is conserved in the RI process.

2. RI with a weak measurement

In our experimental sequence with the dispersive-measurement pulse, the above classic RI is augmented with further evolution from the Kraus operator $\hat{M}(\mathbf{k}_f)$ [see Eq. (4) in the main text] describing the measurement. The final state is therefore

$$|\Psi_f\rangle = \hat{R}_z^\dagger(\delta\phi_P) \hat{R}_y(\pi/2) \hat{R}_z(\delta\phi_P) \hat{M}(\mathbf{k}_f) \hat{R}_y(\pi/2) |\Psi_i\rangle.$$

Our discussion for conventional RI was completely agnostic regarding the initial state. This is not the case with the addition of a measurement pulse. We describe our BEC as containing N atoms in the same spatial mode $\psi(\mathbf{x})$ [with Fourier transform $\tilde{\psi}(\mathbf{k})$], and adopt the notation where

$$\hat{b}^\dagger = \int d^3 \mathbf{x} \psi(\mathbf{x}) \hat{b}^\dagger(\mathbf{x}) = \int \frac{d^3 \mathbf{k}}{(2\pi)^3} \tilde{\psi}(\mathbf{k}) \hat{b}^\dagger(\mathbf{k}) \quad (\text{C3})$$

describes the creation of a single particle in that mode (we will add \uparrow/\downarrow subscripts as needed in what follows). Accordingly our initial state is $|N\rangle = (\hat{b}^\dagger)^N |0\rangle / \sqrt{N!}$ and we will make frequent use of the relation $\hat{b}(\mathbf{k}) |N\rangle = \sqrt{N} \tilde{\psi}(\mathbf{k}) |N-1\rangle$.

An alternate description in terms of coherent states is possible but makes non-physical predictions. In this description the initial state is an eigenstate of the annihilation operator with $\hat{b} |\beta\rangle = \beta |\beta\rangle$ where $N \rightarrow |\beta|^2$ is the average atom number. In the measurement problem, this has the implication that each scattering processes creates a recoiling atom, *but* the number of particles in the condensate mode does not decrease since the action of \hat{b} leaves $|\beta\rangle$ unchanged.

We are interested in the mean number of atoms in momentum state \mathbf{k} and internal state $|\uparrow\rangle$, conditioned on detecting a photon in state \mathbf{k}_\perp :

$$\begin{aligned}
\langle \hat{n}_\uparrow(\mathbf{k}) \rangle_{|\mathbf{k}_\perp} &= \frac{1}{P(\mathbf{k}_\perp)} \langle N | \hat{R}_y^\dagger(\pi/2) \hat{R}_z^\dagger(\delta\phi_P) \hat{M}^\dagger(\mathbf{k}_\perp) R_y^\dagger(\pi/2) \hat{b}_\uparrow^\dagger(\mathbf{k}) \hat{b}_\uparrow(\mathbf{k}) \hat{R}_y(\pi/2) \hat{M}(\mathbf{k}_\perp) \hat{R}_z(\delta\phi_P) \hat{R}_y(\pi/2) | N \rangle \\
&= \frac{1}{2P(\mathbf{k}_\perp)} \langle N | \hat{R}_y^\dagger(\pi/2) \hat{R}_z^\dagger(\delta\phi_P) \hat{M}^\dagger(\mathbf{k}_\perp) [\hat{b}_\uparrow^\dagger(\mathbf{k}) + \hat{b}_\downarrow^\dagger(\mathbf{k})] [\hat{b}_\uparrow(\mathbf{k}) + \hat{b}_\downarrow(\mathbf{k})] \hat{M}(\mathbf{k}_\perp) \hat{R}_z(\delta\phi_P) \hat{R}_y(\pi/2) | N \rangle \\
&\propto \frac{1}{2} \int \frac{d^3\mathbf{k}_1}{(2\pi)^3} \frac{d^3\mathbf{k}_2}{(2\pi)^3} \langle N | \hat{R}_y^\dagger(\pi/2) \left\{ \hat{b}_\uparrow^\dagger(\mathbf{k}_1) \hat{b}_\uparrow[\mathbf{k}_1 - (\mathbf{k}_\perp - \mathbf{k}_0)] \left[e^{-i\delta\phi_P/2} \hat{b}_\uparrow^\dagger(\mathbf{k}) + e^{i\delta\phi_P/2} \hat{b}_\downarrow^\dagger(\mathbf{k}) \right] \right. \\
&\quad \times \left. \left[e^{i\delta\phi_P/2} \hat{b}_\uparrow(\mathbf{k}) + e^{-i\delta\phi_P/2} \hat{b}_\downarrow(\mathbf{k}) \right] \hat{b}_\uparrow^\dagger[\mathbf{k}_2 - (\mathbf{k}_\perp - \mathbf{k}_0)] \hat{b}_\uparrow(\mathbf{k}_2) \right\} \hat{R}_y(\pi/2) | N \rangle. \tag{C5}
\end{aligned}$$

In the last line, we omitted the numerical prefactor for brevity, but will reinstate it at the end of our computation. In the next step we normal order the field operators (with all creation operators moved to the left and the annihilation operators to the right), by performing commutators term-by-term on the chain of field operators inside the curly braces in Eq. (C5) (without the leading and trailing rotation operators). This procedure yields an expression

$$\begin{aligned}
&= \hat{b}_\uparrow^\dagger(\mathbf{k}_1) \left[e^{-i\delta\phi_P/2} \hat{b}_\uparrow^\dagger(\mathbf{k}) + e^{i\delta\phi_P/2} \hat{b}_\downarrow^\dagger(\mathbf{k}) \right] \hat{b}_\uparrow^\dagger[\mathbf{k}_2 - (\mathbf{k}_\perp - \mathbf{k}_0)] \\
&\quad \times \hat{b}_\uparrow[\mathbf{k}_1 - (\mathbf{k}_\perp - \mathbf{k}_0)] \left[e^{i\delta\phi_P/2} \hat{b}_\uparrow(\mathbf{k}) + e^{-i\delta\phi_P/2} \hat{b}_\downarrow(\mathbf{k}) \right] \hat{b}_\uparrow(\mathbf{k}_2) \\
&\quad + \delta(\mathbf{k}_1 - \mathbf{k}_2) \hat{b}_\uparrow^\dagger(\mathbf{k}_1) \left[e^{-i\delta\phi_P/2} \hat{b}_\uparrow^\dagger(\mathbf{k}) + e^{i\delta\phi_P/2} \hat{b}_\downarrow^\dagger(\mathbf{k}) \right] \left[e^{i\delta\phi_P/2} \hat{b}_\uparrow(\mathbf{k}) + e^{-i\delta\phi_P/2} \hat{b}_\downarrow(\mathbf{k}) \right] \hat{b}_\uparrow(\mathbf{k}_2) \\
&\quad + \delta(\mathbf{k}_1 - (\mathbf{k}_\perp - \mathbf{k}_0) - \mathbf{k}) e^{-i\delta\phi_P/2} \hat{b}_\uparrow^\dagger(\mathbf{k}_1) \hat{b}_\uparrow^\dagger[\mathbf{k}_2 - (\mathbf{k}_\perp - \mathbf{k}_0)] \left[e^{i\delta\phi_P/2} \hat{b}_\uparrow(\mathbf{k}) + e^{-i\delta\phi_P/2} \hat{b}_\downarrow(\mathbf{k}) \right] \hat{b}_\uparrow(\mathbf{k}_2) \\
&\quad + \delta(\mathbf{k}_2 - (\mathbf{k}_\perp - \mathbf{k}_0) - \mathbf{k}) e^{i\delta\phi_P/2} \hat{b}_\uparrow^\dagger(\mathbf{k}_1) \left[e^{-i\delta\phi_P/2} \hat{b}_\uparrow^\dagger(\mathbf{k}) + e^{i\delta\phi_P/2} \hat{b}_\downarrow^\dagger(\mathbf{k}) \right] \hat{b}_\uparrow[\mathbf{k}_1 - (\mathbf{k}_\perp - \mathbf{k}_0)] \hat{b}_\uparrow(\mathbf{k}_2) \\
&\quad + \delta(\mathbf{k}_1 - (\mathbf{k}_\perp - \mathbf{k}_0) - \mathbf{k}) \delta(\mathbf{k}_2 - (\mathbf{k}_\perp - \mathbf{k}_0) - \mathbf{k}) \hat{b}_\uparrow^\dagger(\mathbf{k}_1) \hat{b}_\uparrow(\mathbf{k}_2),
\end{aligned}$$

with five terms that we label (I) to (V) from top to bottom. We evaluate each term (now accounting for the rotation operators) by keeping only the operators that act on the initial $|\downarrow\rangle$ state. Integrating over all BEC momentum states \mathbf{k} , we find

$$(I) = \frac{N(N-1)(N-2)}{4} \cos^2 \left(\frac{\delta\phi_P}{2} \right) \left| \int \frac{d^3\mathbf{k}_1}{(2\pi)^3} \tilde{\psi}_\downarrow^*(\mathbf{k}_1) \tilde{\psi}_\downarrow[\mathbf{k}_1 - (\mathbf{k}_\perp - \mathbf{k}_0)] \right|^2, \tag{C6}$$

$$(II) = \frac{N(N-1)}{2} \cos^2 \left(\frac{\delta\phi_P}{2} \right), \tag{C7}$$

$$(III) + (IV) = \frac{N(N-1)}{2} \cos^2 \left(\frac{\delta\phi_P}{2} \right) \left| \int \frac{d^3\mathbf{k}_2}{(2\pi)^3} \tilde{\psi}_\downarrow^*[\mathbf{k}_2 - (\mathbf{k}_\perp - \mathbf{k}_0)] \tilde{\psi}_\downarrow(\mathbf{k}_2) \right|^2, \tag{C8}$$

$$(V) = \frac{N}{4}. \tag{C9}$$

Together terms (I), (III) and (IV) describe collective scattering (the usual Born and Wolf [23] forward scattering from the overall density distribution, as previously noted in Sec. IA) and combine to give

$$(I) + (III) + (IV) = \frac{N(N-1)N}{4} \cos^2 \left(\frac{\delta\phi_P}{2} \right) \left| \int \frac{d^3\mathbf{k}_1}{(2\pi)^3} \tilde{\psi}_\downarrow^*(\mathbf{k}_1) \tilde{\psi}_\downarrow[\mathbf{k}_1 - (\mathbf{k}_\perp - \mathbf{k}_0)] \right|^2. \tag{C10}$$

On the other hand, terms (II) and (V) give

$$(II) + (V) = \frac{N}{2} \left[(N-1) \cos^2 \left(\frac{\delta\phi_P}{2} \right) + \frac{1}{2} \right], \tag{C11}$$

describing independent scattering, i.e., spontaneous emission. These two terms convey that the contrast will be reduced by the fractional count of an atom, i.e. $1/N$, for each spontaneous scattering event.

Finally, we combine all five terms, re-insert the prefactor, integrate over \mathbf{k}_\perp and organize into contributions from single atom scattering P_{sp} and collective scattering P_{col} . This elucidates the distinction between large angle and small

angle scattering, giving

$$\langle \hat{N}_\uparrow(\delta\phi_P) \rangle = \frac{P_{\text{col}}}{P_{\text{tot}}} N \cos^2\left(\frac{\delta\phi_P}{2}\right) + \frac{P_{\text{sp}}}{P_{\text{tot}}} \left[(N-1) \cos^2\left(\frac{\delta\phi_P}{2}\right) + \frac{1}{2} \right], \quad (\text{C12})$$

with total scattering probability P_{tot} . In the first term, small angle collective scattering returns atoms into their initial spatial mode (Mössbauer scattering); thereby leaving the RI contrast unchanged. In the second term, larger angle scattering sends the recoiling atom into a previously empty mode. In this process the environment counts the scattered atom to be in $|\uparrow\rangle$ and removes its contribution to the contrast, as motivated in Sec. III.

Appendix D: Magnetic field lock

Our interferometry measurements operate on the magnetic field sensitive $|F=1, m_F=1\rangle$ to $|F=2, m_F=2\rangle$ transition, and as a result are negatively impacted by magnetic field noise. To minimize any effect on contrast, we monitored the field shifts using a microwave based monitoring scheme first implemented in Ref. [60].

Our two level system is well described by the Hamiltonian

$$\hat{H}_\mu = \frac{\hbar}{2} \begin{pmatrix} \Delta_\mu + \delta_\mu & \Omega_\mu \\ \Omega_\mu & -(\Delta_\mu + \delta_\mu) \end{pmatrix},$$

where Δ_μ describes an unknown detuning from resonance, δ_μ is an adjustable detuning, and Ω_μ is the microwave Rabi frequency.

Our protocol began with optically trapped atoms just above T_c in the $|F=1, m_F=1\rangle$ hyperfine state. We applied a microwave pulse of duration $t_\mu = 100 \mu\text{s}$ and Rabi frequency $\Omega_\mu/(2\pi) \approx 0.1/t_\mu$ detuned by $\delta_\mu/(2\pi) = 1/(2t_\mu) = 5 \text{ kHz}$ from resonance and absorption-imaged the atoms transferred to $|F=2, m_F=2\rangle$ in-situ ($\approx 10\%$ fractional transfer) leaving $|F=1, m_F=1\rangle$ state atoms undisturbed. We used these data to obtain the transferred atom number N_+ . Then after a $\approx 34 \text{ ms}$ delay, we repeated the processes with $\delta \rightarrow -\delta$, giving N_- . The delay between the transfer pulses was selected to be an

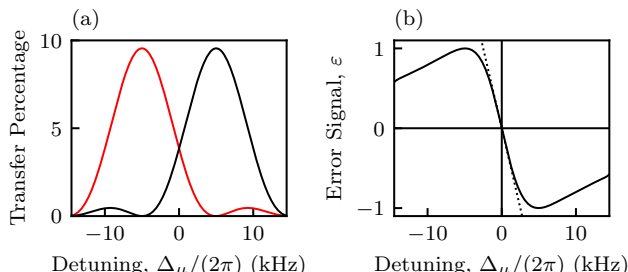


FIG. 7. Microwave field lock. (a) Transfer fraction for individual pulses with parameters as described in the text. (b) Error function (solid curve) and linear approximation (dashed line).

integer multiple of the $T_{\text{line}} = (60 \text{ Hz})^{-1} \approx 17 \text{ ms}$ line period.

The fractional imbalance between the transferred numbers

$$\epsilon = \frac{N_+ - N_-}{N_+ + N_-} \approx -4t_\mu \frac{\Delta_\mu}{2\pi}, \quad (\text{D1})$$

provides an error signal that can be related to any overall shift in detuning Δ_μ . For example $\epsilon = 0.5$ corresponds to a detuning of just $\Delta_\mu/2\pi \approx 1.25 \text{ kHz}$.

We employed a two step procedure to minimize the impact of field noise during on interferometry experiments. First, prior to any measurement sequence we optimized the bias field to minimize δB . Second, we post-selected data to exclude cases with $|\epsilon| > 0.5$; this value was determined empirically to retain most of the data while notably removing outliers in measured contrast.

Appendix E: Lattice pulse sequence

An intuitive picture of our scheme for mitigating the effect of the optical lattice begins with a three-state truncation [37, 38] of the full lattice Hamiltonian

$$\frac{\hat{H}(k)}{E_0} = \begin{pmatrix} (k+2k_0)^2 & s/4 & 0 \\ s/4 & k^2 & s/4 \\ 0 & s/4 & (k-2k_0)^2 \end{pmatrix}, \quad (\text{E1})$$

describing a lattice of depth sE_0 , with single photon recoil momentum $\hbar k_0 = 2\pi\hbar/\lambda$, energy $E_0 = \hbar^2 k_0^2/(2m)$, and time $T_0 = 2\pi\hbar/E_0 \approx 265 \mu\text{s}$. For atoms initially at rest, i.e. $k=0$, this is a resonant lambda coupling scheme with bright state subspace spanned by $|b_0\rangle = |k=0\rangle$ and $|b_1\rangle = (|k=-2k_0\rangle + |k=2k_0\rangle)/\sqrt{2}$ and an uncoupled dark state $|d\rangle = (|k=-2k_0\rangle - |k=2k_0\rangle)/\sqrt{2}$.

Since our initial state $|k=0\rangle$ is in the bright state manifold, we focus on the bright state Hamiltonian

$$\frac{\hat{H}_b(0)}{E_0} = \begin{pmatrix} 0 & s/(2\sqrt{2}) \\ s/(2\sqrt{2}) & 4 \end{pmatrix} = 2\hat{I} + \frac{1}{2} \left[4\hat{\sigma}_z + \frac{s}{\sqrt{2}}\hat{\sigma}_x \right]. \quad (\text{E2})$$

When the lattice is off, this Hamiltonian describes Larmor procession around \mathbf{e}_z with Rabi frequency $4E_0/\hbar$ and when the lattice is on it describes procession about $4\mathbf{e}_z + [s/\sqrt{2}]\mathbf{e}_x$ with Rabi frequency $\sqrt{16 + s^2/2E_0}/\hbar$. In the limit $s \ll 4\sqrt{2}$, the axis of rotation is tipped by $\theta = 4s/\sqrt{2}$, and the Rabi frequency is nearly unchanged from $4E_0/\hbar$. The dashed lines in Fig. 8(a) plot the top of

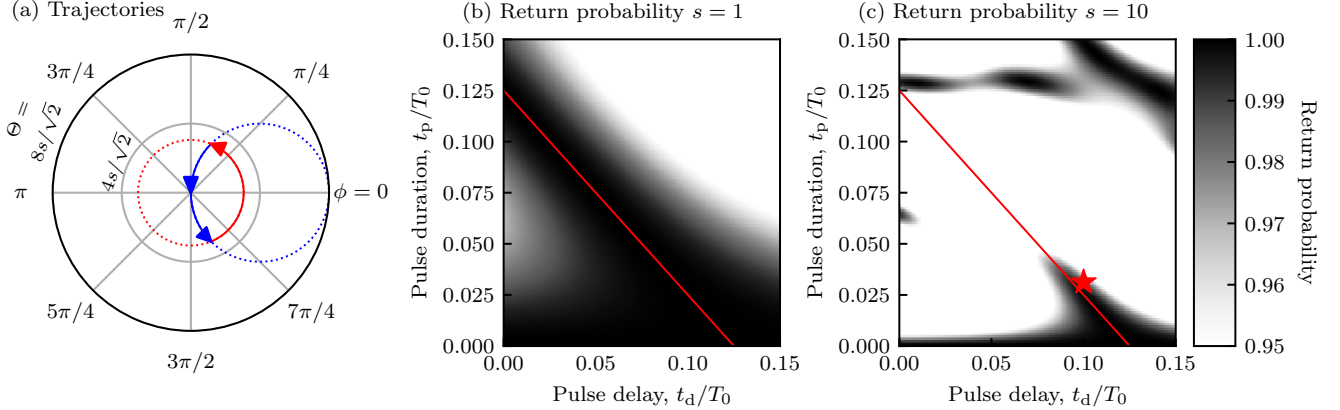


FIG. 8. Lattice pulse sequence. (a) Top of Bloch sphere for the spherical polar angles ϕ and θ showing trajectories for zero (red) and non-zero (blue) s . The dashed curve shows complete orbits while the solid curve with arrows results from a pulsed sequence that combine to form trajectory that returns to the initial state. (b) and (c) Return probability computed including 7 momentum states for $s = 1$ and $s = 10$. The star marks the parameters used in our experiment.

the Bloch sphere with two example orbits in this limit, both for zero (red) and non-zero s (blue).

The solid curves in Fig. 8(a) show the trajectory for a two pulse sequence that also returns to the origin. In the small s limit, the condition to return to the initial state is $t_d/T_0 = 1/16 - t_p/T_0$, where t_d is the delay time between pulses and t_p is the pulse duration. Figure 8(b) plots the probability that the final state returns to $k = 0$ for a shallow lattice with $s = 1$ (computed using 7 momentum states). The red line indicates the predicted minimum which is in good agreement with the numerically evaluated optimum configuration.

Figure 8(c) plots the same quantity, now with $s = 10$, showing the narrow range of parameters for which our scheme is expected to be successful. For most parameters, the large s simulation is qualitatively different from the small s results, with the exception of very short pulse times and the region following our scheme. In practice we selected $t_d = T_0/10 = 26.5 \mu\text{s}$ and $t_p = T_0/32 = 8.2 \mu\text{s}$, marked by the red star in (c).

Appendix F: Bolometry

1. Image analysis: number and temperature extraction

Standard absorption imaging begins with an image I_A containing the shadow of the atomic ensemble in a large probe beam and a second image I_P with the atoms absent. The analysis begins by computing the ratio of these two images $f = I_A/I_P$. Both of these images contain diffraction fringes from dust and imperfections in the imaging system. These imperfections can move on the wavelength scale in the time between the acquisition of the images, meaning that f can contain spurious modulations from phase-shifted interference structures. We use a principle component analysis (PCA) based technique to generate an “optimal” probe I_{PCA} for each I_A

to remove these artifacts. In some data f differs slightly from 1 in regions where no atoms are present, giving an artificial background that we remove. We then computed the I_{sat} corrected optical depth

$$\text{OD}' = -\ln\left(\frac{I_A}{I_{\text{PCA}}}\right) - \frac{I_A - I_{\text{PCA}}}{I_{\text{sat}}}; \quad (\text{F1})$$

for further discussion see Ref. [31].

We then extract temperature by excluding the central region (containing the Bose-condensed atoms) and performing a fit of the remainder to a 2D Gaussian model

$$G(x, y) = a_g \exp\left[-\frac{1}{2} \sum_{i=x,y} \left(\frac{x_i - b_i}{\sigma_i}\right)^2\right], \quad (\text{F2})$$

where a_g is the amplitude, $\sigma_{x,y}$ are the widths, and $b_{x,y}$ are center positions. We implemented the exclusion by assigning extremely large uncertainties to data within the exclusion region. The width of the excluded region along each direction was set to be 5 % larger than the largest observed Thomas-Fermi radius along that direction. Since $\omega_y \approx 14.9 \times \omega_x$, the excluded region was elliptical.

In our fits the widths σ_x and σ_y vary independently, and as such we obtain two measures of temperature

$$T_{x,y} = \frac{m}{k_B} \frac{\omega_{x,y}^2}{1 + \omega_{x,y}^2 t^2} \sigma_{x,y}^2, \quad (\text{F3})$$

where t is the TOF duration. In our anisotropic trap (with $\omega_x \ll \omega_y, \omega_z$) the *in situ* extent of our clouds along \mathbf{e}_x were not small compared to the size in TOF. As such T_x has an $\approx 10\%$ correction compared to the long TOF limit whereas the correction for T_y is negligible. In addition the quadrupole magnetic field used for the Stern-Gerlach gradient introduces curvature terms along \mathbf{e}_x , increasing the x -width of $|F = 1, m_F = 1\rangle$ distributions and reducing that of $|F = 2, m_F = 2\rangle$ distributions. In

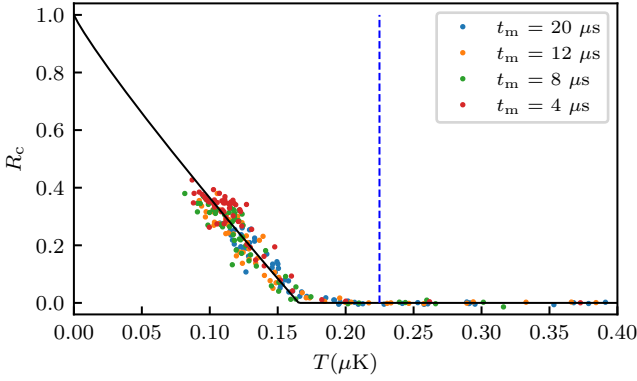


FIG. 9. Determination of critical temperature. The vertical blue dashed line marks the predicted T_c^0 for non-interacting bosons computed from for our trap frequencies in the compressed trap and total atom number N_{nm} .

past experiments, this was observed to be an $\lesssim 5\%$ effect. Since T_y requires no correction factors, it would be favored as our primary measure of T . However, we observed systematic shifts of T_y (and not T_x) between different thermal gas measurement runs, for which T_x and T_y were not in agreement with each other, and as such we report $T = T_x$.

The number of atoms in thermal component is determined by integrating over the Gaussian profile, giving $N_{\text{nc}} = 2\pi\sigma_x\sigma_ya_g/\sigma_0$. Here σ_0 is the resonant scattering cross-section. To obtain the condensate population N_c we integrate the excluded region after subtracting the fitted thermal profile.

2. BEC Thermodynamics

The per-particle energy for a weakly interacting BEC given in Eq. (6) requires the knowledge of two critical experimental parameters: 3D non-interacting BEC transition temperature T_c^0 and the chemical potential μ . This appendix provides the analysis details for obtaining each parameter.

In order to determine T_c^0 we first extract the critical temperature T_c by fitting the observed condensate fraction R_c to

$$R_c = \max \left[1 - \left(\frac{T}{T_c} \right)^a, 0 \right], \quad (\text{F4})$$

where T_c and a are fit parameters. Figure 9 presents the measured R_c as a function of T , where the best fit results are $T_c = 165(10)$ nK and $a = 0.90(1)$. Owing to the reduction of T_c with respect to the 3D non-interacting value, for the energy computation we use T_c^0 acquired from our observed T_c following Eq. (119) of Ref. [25]:

$$\frac{\delta T_c}{T_c^0} = -1.3 \frac{a_{\text{Rb}}}{a_{\text{ho}}} N^{1/6}, \quad (\text{F5})$$

where the shift in the critical temperature is $\delta T_c = T_c - T_c^0$; a_{Rb} is the ^{87}Rb scattering length; $a_{\text{ho}} = (\hbar/m\omega_{\text{ho}})$ is

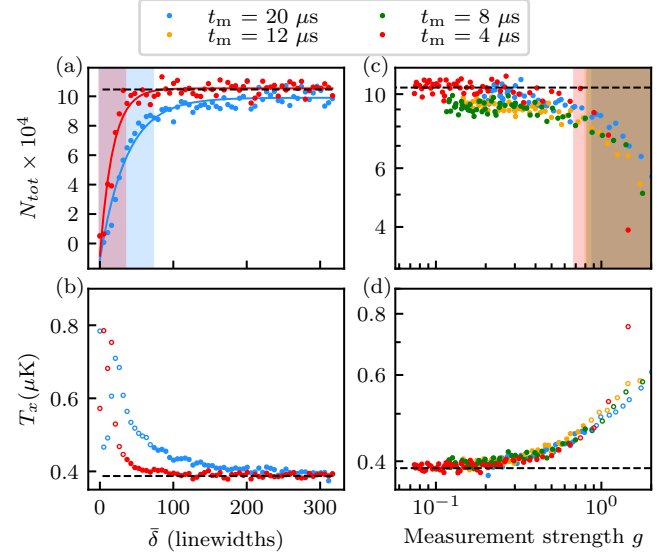


FIG. 10. Measurement induced heating of a thermal gas. Left: Results for measurement times $t_m = 4\ \mu\text{s}$ and $20\ \mu\text{s}$ plotted as a function of $\bar{\delta}$. Right: Data plotted as a function of g on logarithmic scale, with data excluded as described in the text plotted with hollow symbols. (a), (c) Total number N_t . The solid curves in (a) are fits to a rising exponential function and the shaded regions are where N_t has fallen below 85 % of its asymptotic value. (b), (d) Temperature T . The dashed black lines depict the results where no weak measurement was performed. Each data point is the average of 5 iterations of the experiment.

the harmonic oscillator length with the geometric mean of trap frequencies $\omega_{\text{ho}} = (\omega_x\omega_y\omega_z)^{1/3}$. For the no-weak-measurement BEC results (dashed lines in Fig. 5) we determine the number of atoms to be $N_{\text{nm}} = 0.61(15) \times 10^5$. For our compressed ODT configuration, Eq. (F5) yields $T_c^0 = 225$ nK.

According to the Thomas-Fermi approximation, the chemical potential is related to the condensed atom number by

$$\mu = \frac{\omega_{\text{ho}}}{2} \left[\frac{15Na_{\text{Rb}}}{a_{\text{ho}}} \right]^{2/5}. \quad (\text{F6})$$

We derive the chemical potential μ using N_{nm} value with the measured compressed trap frequencies.

3. Measurement Induced Heating in a Thermal Gas

We made complementary measurements in a dilute thermal gas to study the change in temperature due to dispersive measurements. Fig. 10 displays the observed change in N_t and T as we adjusted g by varying the probe beam detuning $\bar{\delta}$ for different measurement times t_m . Similar to the BEC measurements reported in Fig. 5, panels (c)-(d) demonstrate that N_t and T collapse when scaled to g .

[1] H. J. Carmichael, Quantum trajectory theory for cascaded open systems, *Phys. Rev. Lett.* **70**, 2273 (1993).

[2] K. Mølmer, Y. Castin, and J. Dalibard, Monte carlo wave-function method in quantum optics, *J. Opt. Soc. Am. B* **10**, 524 (1993).

[3] C. L. Degen, F. Reinhard, and P. Cappellaro, Quantum sensing, *Rev. Mod. Phys.* **89**, 035002 (2017).

[4] K. Hammerer, A. S. Sørensen, and E. S. Polzik, Quantum interface between light and atomic ensembles, *Rev. Mod. Phys.* **82**, 1041 (2010).

[5] B. M. Terhal, Quantum error correction for quantum memories, *Rev. Mod. Phys.* **87**, 307 (2015).

[6] H. Krauter, C. A. Muschik, K. Jensen, W. Wasilewski, J. M. Petersen, J. I. Cirac, and E. S. Polzik, Entanglement generated by dissipation and steady state entanglement of two macroscopic objects, *Phys. Rev. Lett.* **107**, 080503 (2011).

[7] M. J. Gullans and D. A. Huse, Dynamical purification phase transition induced by quantum measurements, *Phys. Rev. X* **10**, 041020 (2020).

[8] C. Noel, P. Niroula, D. Zhu, A. Risinger, L. Egan, D. Biswas, M. Cetina, A. V. Gorshkov, M. J. Gullans, D. A. Huse, and C. Monroe, Measurement-induced quantum phases realized in a trapped-ion quantum computer, *Nature Physics* **18**, 760 (2022).

[9] M. Block, Y. Bao, S. Choi, E. Altman, and N. Y. Yao, Measurement-induced transition in long-range interacting quantum circuits, *Phys. Rev. Lett.* **128**, 010604 (2022).

[10] I. Bloch, J. Dalibard, and W. Zwerger, Many-body physics with ultracold gases, *Rev. Mod. Phys.* **80**, 885 (2008).

[11] M. Müller, S. Diehl, G. Pupillo, and P. Zoller, Engineered open systems and quantum simulations with atoms and ions, in *Advances in Atomic, Molecular, and Optical Physics*, Vol. 61, edited by P. Berman, E. Arimondo, and C. Lin (Academic Press, 2012) pp. 1–80.

[12] A. B. Deb and N. Kjærgaard, Observation of pauli blocking in light scattering from quantum degenerate fermions, *Science* **374**, 972 (2021).

[13] C. Sanner, L. Sonderhouse, R. B. Hutson, L. Yan, W. R. Milner, and J. Ye, Pauli blocking of atom-light scattering, *Science* **374**, 979 (2021).

[14] Y. Margalit, Y.-K. Lu, F. c. Top, and W. Ketterle, Pauli blocking of light scattering in degenerate fermions, *Science* **374**, 976 (2021).

[15] Y.-K. Lu, Y. Margalit, and W. Ketterle, Observation of bosonic stimulation in light scattering, arXiv preprint arXiv:2204.06639 (2022).

[16] M. R. Andrews, M.-O. Mewes, N. J. van Druten, D. S. Durfee, D. M. Kurn, and W. Ketterle, Direct, nondestructive observation of a bose condensate, *Science* **273**, 84 (1996).

[17] A. Ramanathan, S. R. Muniz, K. C. Wright, R. P. Anderson, W. D. Phillips, K. Helmerson, and G. K. Campbell, Partial-transfer absorption imaging: A versatile technique for optimal imaging of ultracold gases, *Review of Scientific Instruments* **83**, 083119 (2012).

[18] D. V. Freilich, D. M. Bianchi, A. M. Kaufman, T. K. Langan, and D. S. Hall, Real-time dynamics of single vortex lines and vortex dipoles in a bose-einstein condensate, *Science* **329**, 1182 (2010).

[19] M. Gajdacz, P. L. Pedersen, T. Mørch, A. J. Hilliard, J. Arlt, and J. F. Sherson, Non-destructive Faraday imaging of dynamically controlled ultracold atoms, *Review of Scientific Instruments* **84**, 83105 (2013).

[20] E. Altuntas and I. B. Spielman, Self-bayesian aberration removal via constraints for ultracold atom microscopy, *Phys. Rev. Research* **3**, 043087 (2021).

[21] J. M. Higbie, L. E. Sadler, S. Inouye, A. P. Chikkatur, S. R. Leslie, K. L. Moore, V. Savalli, and D. M. Stamper-Kurn, Direct nondestructive imaging of magnetization in a spin-1 bose-einstein gas, *Phys. Rev. Lett.* **95**, 050401 (2005).

[22] L. E. Sadler, J. M. Higbie, S. R. Leslie, M. Vengalattore, and D. M. Stamper-Kurn, Coherence-enhanced imaging of a degenerate bose-einstein gas, *Phys. Rev. Lett.* **98**, 110401 (2007).

[23] M. Born and E. Wolf, *Principles of Optics: Electromagnetic Theory of Propagation, Interference and Diffraction of Light* (7th Edition), 7th ed. (Cambridge University Press, 1999).

[24] All uncertainties herein reflect the uncorrelated combination of single-sigma statistical and systematic uncertainties.

[25] F. Dalfovo, S. Giorgini, L. P. Pitaevskii, and S. Stringari, Theory of bose-einstein condensation in trapped gases, *Rev. Mod. Phys.* **71**, 463 (1999).

[26] Y. Castin and R. Dum, Bose-einstein condensates in time dependent traps, *Phys. Rev. Lett.* **77**, 5315 (1996).

[27] The long TOF period was 20 ms; the absorption imaging pulse was 20 μ s in duration and had intensity $I/I_{\text{sat}} \approx 1$, where $I_{\text{sat}} \approx 1.67 \text{ mW/cm}^2$.

[28] Here we directly count the atom number within a 1 recoil momentum circle centered on the BEC.

[29] A. Fuhrmanek, R. Bourgain, Y. R. P. Sortais, and A. Browaeys, Light-assisted collisions between a few cold atoms in a microscopic dipole trap, *Phys. Rev. A* **85**, 062708 (2012).

[30] The Stark shift of $|g_1\rangle$ is a small contribution that we nonetheless include in our fits.

[31] G. Reinaudi, T. Lahaye, Z. Wang, and D. Guéry-Odelin, Strong saturation absorption imaging of dense clouds of ultracold atoms, *Opt. Lett.* **32**, 3143 (2007).

[32] K. Hueck, N. Luick, L. Sobirey, J. Siegl, T. Lompe, H. Moritz, L. W. Clark, and C. Chin, Calibrating high intensity absorption imaging of ultracold atoms, *Opt. Express* **25**, 8670 (2017).

[33] E. Altuntas and I. B. Spielman, Primary calibration of laser intensity via ramsey interferometry, In preparation (2022).

[34] We imaged the *in situ* probe beam (with no atoms present) on a charge coupled device camera to obtain the local probe intensity (in arbitrary camera units) at the location of the BEC. Further details are described in Ref. [33].

[35] J. Appel, P. J. Windpassinger, D. Oblak, U. B. Hoff, N. Kjærgaard, and E. S. Polzik, Mesoscopic atomic entanglement for precision measurements beyond the standard quantum limit, *Proceedings of the National Academy of Sciences* **106**, 10960 (2009).

[36] The probe beam is nearly perfectly concentric with our imaging system and intersects each optical element at normal incidence. While it is common practice in optical setups to slightly tilt optical elements to eliminate back-reflections, in the high-resolution imaging context optimized alignment is a necessary condition for minimizing optical aberrations.

[37] S. Wu, Y.-J. Wang, Q. Diot, and M. Prentiss, Splitting matter waves using an optimized standing-wave light-pulse sequence, *Phys. Rev. A* **71**, 43602 (2005).

[38] C. D. Herold, V. D. Vaidya, X. Li, S. L. Rolston, J. V. Porto, and M. S. Safronova, Precision measurement of transition matrix elements via light shift cancellation, *Phys. Rev. Lett.* **109**, 243003 (2012).

[39] W. Ketterle, D. S. Durfee, and D. Stamper-Kurn, Bose-Einstein condensation in atomic gases, proceedings of the international school of physics “Enrico Fermi”, course CXL (IOS Press, 1999) Chap. Making, probing and understanding Bose-Einstein condensates, pp. 67–176.

[40] J. Szczepkowski, R. Gartman, M. Witkowski, L. Tracewski, M. Zawada, and W. Gawlik, Analysis and calibration of absorptive images of bose-einstein condensate at nonzero temperatures, *Review of Scientific Instruments* **80**, 053103 (2009), <https://doi.org/10.1063/1.3125051>.

[41] For BECs, unlike the thermal gas case, the scattering process adds both kinetic and interaction energy. For our small condensate fraction the interaction energy is not a significant contributor.

[42] R. Olf, F. Fang, G. E. Marti, A. MacRae, and D. M. Stamper-Kurn, Thermometry and cooling of a bose gas to 0.02 times the condensation temperature, *Nature Physics* **11**, 720 (2015).

[43] T. Y. Ivanova and D. A. Ivanov, Quantum limits of feedback cooling in optical lattices, *Journal of Experimental and Theoretical Physics Letters* **82**, 482 (2005).

[44] M. Koch, C. Sames, A. Kubanek, M. Apel, M. Balbach, A. Ourjoumtsev, P. W. H. Pinkse, and G. Rempe, Feedback cooling of a single neutral atom, *Phys. Rev. Lett.* **105**, 173003 (2010).

[45] N. Behbood, G. Colangelo, F. Martin Ciurana, M. Napolitano, R. J. Sewell, and M. W. Mitchell, Feedback cooling of an atomic spin ensemble, *Phys. Rev. Lett.* **111**, 103601 (2013).

[46] L. Walker, *Measurement and control of atomic and nanomechanical systems for quantum technologies*, Ph.D. thesis, University of Strathclyde (2020).

[47] J. T. Young, A. V. Gorshkov, and I. B. Spielman, Feedback-stabilized dynamical steady states in the bose-hubbard model, *Phys. Rev. Research* **3**, 043075 (2021).

[48] S. Diehl, A. Tomadin, A. Micheli, R. Fazio, and P. Zoller, Dynamical phase transitions and instabilities in open atomic many-body systems, *Phys. Rev. Lett.* **105**, 015702 (2010).

[49] N. S. Kampel, A. Griesmaier, M. P. H. Steenstrup, F. Kaminski, E. S. Polzik, and J. H. Müller, Effect of light assisted collisions on matter wave coherence in superradiant bose-einstein condensates, *Phys. Rev. Lett.* **108**, 090401 (2012).

[50] A. Urvoy, Z. Vendeiro, J. Ramette, A. Adiyatullin, and V. Vuletić, Direct laser cooling to bose-einstein condensation in a dipole trap, *Phys. Rev. Lett.* **122**, 203202 (2019).

[51] W. Ketterle and M. W. Zwierlein, Making, probing and understanding ultracold fermi gases, *Rivista del Nuovo Cimento* **31**, 247 (2008).

[52] K. C. Cox, G. P. Greve, J. M. Weiner, and J. K. Thompson, Deterministic squeezed states with collective measurements and feedback, *Phys. Rev. Lett.* **116**, 93602 (2016).

[53] O. Hosten, N. J. Engelsen, R. Krishnakumar, and M. A. Kasevich, Measurement noise 100 times lower than the quantum-projection limit using entangled atoms, *Nature* **529**, 505 (2016).

[54] J. Zeiher, J. Wolf, J. A. Isaacs, J. Kohler, and D. M. Stamper-Kurn, Tracking evaporative cooling of a mesoscopic atomic quantum gas in real time, *Phys. Rev. X* **11**, 041017 (2021).

[55] B. P. Anderson, P. C. Haljan, C. A. Regal, D. L. Feder, L. A. Collins, C. W. Clark, and E. A. Cornell, Watching dark solitons decay into vortex rings in a bose-einstein condensate, *Phys. Rev. Lett.* **86**, 2926 (2001).

[56] H. Pichler, A. J. Daley, and P. Zoller, Nonequilibrium dynamics of bosonic atoms in optical lattices: Decoherence of many-body states due to spontaneous emission, *Phys. Rev. A* **82**, 063605 (2010).

[57] J. Schachenmayer, L. Pollet, M. Troyer, and A. J. Daley, Spontaneous emission and thermalization of cold bosons in optical lattices, *Phys. Rev. A* **89**, 011601 (2014).

[58] C. M. Caves and G. J. Milburn, Quantum-mechanical model for continuous position measurements, *Phys. Rev. A* **36**, 5543 (1987).

[59] T. A. Brun, A simple model of quantum trajectories, *American Journal of Physics* **70**, 719 (2002).

[60] L. J. LeBlanc, M. C. Beeler, K. Jiménez-García, A. R. Perry, S. Sugawa, R. A. Williams, and I. B. Spielman, Direct observation of zitterbewegung in a bose-einstein condensate, *New Journal of Physics* **15**, 073011 (2013).